Flow Disturbance Characterization Measurements in the National Transonic Facility (Invited)

Rudolph A. King*, Marlyn Y. Andino*, Latunia Melton†,
Flow Physics and Control Branch, NASA Langley Research Center, Hampton, VA 23681

Jenna Eppink‡,
Computational Aerosciences Branch, NASA Langley Research Center, Hampton, VA 23681

Michael A. Kegerise§, and Andrew Tsoi¶
Flow Physics and Control Branch, NASA Langley Research Center, Hampton, VA 23681

Recent flow measurements have been acquired in the National Transonic Facility (NTF) to assess the unsteady flow environment in the test section. The primary purpose of the test is to determine the feasibility of the NTF to conduct laminar-flow-control testing and boundary-layer transition sensitive testing. The NTF can operate in two modes, warm (air) and cold/cryogenic (nitrogen) test conditions for testing full and semispan scaled models. The warm-air mode enables low to moderately high Reynolds numbers through the use of high tunnel pressure, and the nitrogen mode enables high Reynolds numbers up to flight conditions, depending on aircraft type and size, utilizing high tunnel pressure and cryogenic temperatures. NASA's Environmentally Responsible Aviation (ERA) project is interested in demonstrating different laminar-flow technologies at flight-relevant operating conditions throughout the transonic Mach number range and the NTF is well suited for the initial ground-based demonstrations. In the current test, we acquired data for Mach and unit Reynolds numbers ranging from $0.2 \leq M \leq 0.95$ and $3.3 \times 10^6 < Re/m < 220 \times 10^6$ ($1 \times 10^6 < Re/ft < 67 \times 10^6$) collectively at air and cryogenic conditions. Measurements were made in the test section using a survey rake that was populated with 19 probes. Roll polar data at selected test conditions were obtained to look at the uniformity of the flow disturbance field in the test section. Data acquired from the rake probes included mean total temperatures, mean and fluctuating static/total pressures, and mean and fluctuating hot-wire measurements. The results presented in this report focus primarily on the unsteady pressure and hot-wire results in the form of $\langle P'_s \rangle / q$, $\langle m' \rangle / (\bar{m})$, etc. Based on the current measurements and previous data, an assessment was made that the NTF is a suitable facility for ground-based demonstrations of laminar-flow technologies at flight-relevant conditions in the cryogenic mode.

Nomenclature

A	hot-wire calibration coefficient (see Eq. 8)
a	speed of sound
B	hot-wire calibration coefficient (see Eq. 8)
d	hot-wire sensor diameter, 5 μm
l	active hot-wire sensor length, 1.25 mm
M	Mach number
m	massflux, ρu

*Research Engineer, M.S. 170. Member, AIAA.
†Research Engineer, M.S. 170. Associate Fellow, AIAA.
‡Graduate Student, M.S. 128. Student Member, AIAA.
§Research Engineer, M.S. 170. Senior Member, AIAA.
¶Student Trainee, University of Colorado at Boulder.

Nu	Nusselt number
P	pressure
Pr	Prandtl number
q	dynamic pressure
R	ideal gas constant, (air: 286.9 J/kg·K, N_2: 296.8 J/kg·K)
Re	Reynolds number
Re_t	wire Reynolds number based on stagnation conditions, $\frac{\rho u d}{\mu_t}$
r	radial distance along rake
S_χ	hot-wire sensitivity to generic flow variable χ, $\frac{\chi}{E}\frac{\partial E}{\partial \chi}$
T	temperature
T_e	wire recovery temperature
Tu	turbulence intensity, $\langle u' \rangle / \bar{u}$
T_w	wire temperature
u	velocity
ϕ	rake roll angle
γ	specific heat ratio
η	recovery factor, T_e/T_t
μ	viscosity
ρ	density
σ	standard deviation
τ	overheat ratio, $(T_w - T_e)/T_t$
τ_o	time delay

Subscript

s	static conditions
t	total (stagnation) conditions

Superscript

n	hot-wire calibration exponent, $n = 0.5$ (see Eq. 8)
$\bar{(\ )}$	= mean value
$(\ )'$	= unsteady component
$\langle\ \rangle$	$= \sqrt{\overline{(\ )^2}}$, root-mean-square (rms) value

I. Introduction

The National Transonic Facility (NTF) at NASA Langley Research Center has the capability of operating at high Reynolds numbers and Mach numbers relevant to transport configurations.[1–4] The NTF was conceived based on the need for high Reynolds number test capabilities to support future aerospace vehicle systems. The NTF became operational in 1984; since that time, a range of investigations have been conducted in the facility. The NTF is capable of achieving a maximum unit Reynolds number of 480×10^6/m (146×10^6/ft). For some time, this was a unique asset in the world. Later in the 1990's, a second facility outside of the United States, the European Transonic Wind Tunnel (ETW),[5,6] became operational with a maximum unit Reynolds number range of approximately 220×10^6/m (67×10^6/ft). These two large-scale transonic wind tunnels are the only two high Reynolds number facilities that exist in the world today capable of testing at flight-relevant transport test conditions. Both tunnels achieve high Reynolds numbers based on pressurization, size, and cryogenics (gaseous nitrogen as the working fluid).

NASA's Environmentally Responsible Aviation (ERA) project[7,8] has identified as one of its goals a 50% fuel burn reduction below the current state-of-the-art aircraft. Technologies that result in aerodynamic drag reduction are a partial solution to meeting the goal; laminar flow control (LFC)[9] is a promising technology in this group. Laminar flow control via active chordwise suction has been demonstrated for some years as a means to reduce skin friction,[10] but has proved difficult to achieve on swept wings at high Reynolds numbers

in an operational environment. Due to overall system penalties associated with suction systems, hybrid LFC (HLFC)[11] that combines flow control near the leading edge for control of attachment-line and/or crossflow instabilities and natural LFC (NLFC) for control of Tollmien-Schlichting instabilities is the approach of choice. HLFC has been shown through ERA system studies to provide approximately 9.9% in fuel burn reduction for a tube + wing configuration.[7]

Part of ERA's focus is to mature these technologies to meet technology readiness level of 6 by 2020. To achieve this focus for LFC activities, the ability to conduct laminar-flow-control and boundary-layer transition sensitive testing at flight-relevant conditions for scaled models in a ground-based facility is desired. In addition, high Reynolds number ground-based capabilities are needed to provide the necessary confidence in the ground-test phase of production development for commercial and governmental customers. For these reasons, the high Reynolds number capability of the NTF makes it a viable facility. However, we need to have a better understanding of the unsteady disturbance environment in the test section to decide if the facility can be qualified for laminar flow demonstrations. Igoe[12] made extensive fluctuating static pressure measurements at several locations throughout the circuit of the NTF for warm and cold conditions. He found that the NTF has low levels of fluctuating unsteady pressures relative to other transonic wind tunnels, especially for high subsonic Mach numbers of 0.7 to 0.9. He identified spectral peaks in the settling chamber power spectra that were attributed to the vortex shedding from the heat exchanger and associated support structure. Previous NTF unsteady flow quality measurements by McGinley et al.[13] and later by Wlezien et al.[14] that utilized hot wires and unsteady pressures indicate $\%Tu \approx 0.3$ and below. These data were acquired both at warm (dry air) and cryogenic (gaseous nitrogen) conditions with sensors that were fixed spatially to both sidewalls. Wlezien et al. found that the general trend of the facility is a reduction in turbulence levels for cryogenic conditions. They also speculated on the role of the heat exchanger (which is only used in the air mode) in introducing temperature spottiness into the flow for air-mode testing. To date, no direct measurements at high Reynolds numbers in the cryogenic mode (preferred mode of operation), have been made to determine the spatial uniformity of the disturbance field in the NTF test section. However, a recent collaborative test by Boeing and NASA (Crouch et al.[15]) on a transonic wing at high Reynolds number cryogenic conditions was conducted to indirectly assess NTF's flow quality. Based on the extent of laminar flow, they estimated $\%Tu \approx 0.24$ using the method of Mack.[16] They concluded that the NTF is an acceptable facility for laminar-flow testing provided bypass transition due to minute particulates is avoided. The presence of minute particulates can be particularly destabilizing in flows where crossflow exists and is being investigated in a separate study.

The objective of this test (Test 203) is to determine the feasibility of the NTF to conduct LFC testing. We approached this study by making direct measurements of the unsteady flow field in the test section at both warm and cold conditions. The test was conducted using the NTF survey rake so that we could investigate any spatial distribution of the disturbance environment within the NTF test section. We first discuss the experimental details to include the facility, survey rake, measurement probes, instrumentation and general measurement reduction approach. We continue with the presentation of results for both operational modes, warm and cold, over a range of test conditions and then conclude by summarizing comments.

II. Experimental Details

A. Facility and Model

The test was conducted in the National Transonic Facility to achieve high flight-relevant Reynolds numbers at transonic conditions appropriate for sub-scale models. The high Reynolds numbers are achieved with a combination of high pressures, cryogenic temperatures and size. The NTF is a closed-circuit fan-driven tunnel with a 15:1 contraction ratio. Test gas is either dry air (warm mode) or nitrogen (cold mode) with a temperature range of 78 K (-320 °F) to 339 K (150 °F). The test section is 2.5-m (8.2-ft) square with a length of 7.6 m (25 ft). The Mach number range and pressure range are approximately 0.1 to 1.2 and 103 kPa (15 psia) to 860 kPa (125 psia), respectively. The tunnel is capable of achieving a maximum unit Reynolds number of 480×10^6/m (146×10^6/ft) at $M = 1$ and a maximum dynamic pressure of up to $q = 335$ MPa (7000 psf). Additional details on the NTF are available in the following references.[1–4]

The current measurements were acquired at three nominal temperatures, 322 K (120 °F), 172 K (-150 °F), and 116 K (-250 °F), that consist of one air-mode operation and two nitrogen-mode operations. Measurements were made in the test section for a Mach number range of $0.2 \leq M \leq 0.95$ and unit Reynolds number range of $3.3 \times 10^6 < Re/\text{m} < 220 \times 10^6$ ($1 \times 10^6 < Re/\text{m} < 67 \times 10^6$). The maximum dynamic pressure was

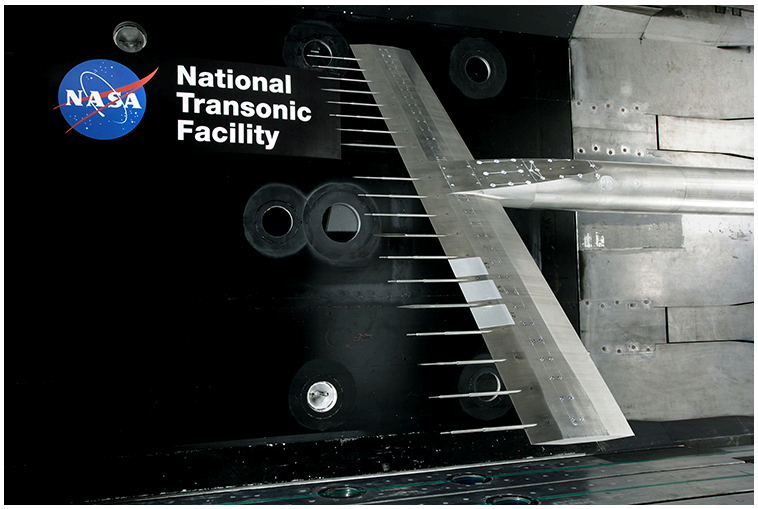

Figure 1: **Photograph of 7-foot rake installed in the NTF test section.**

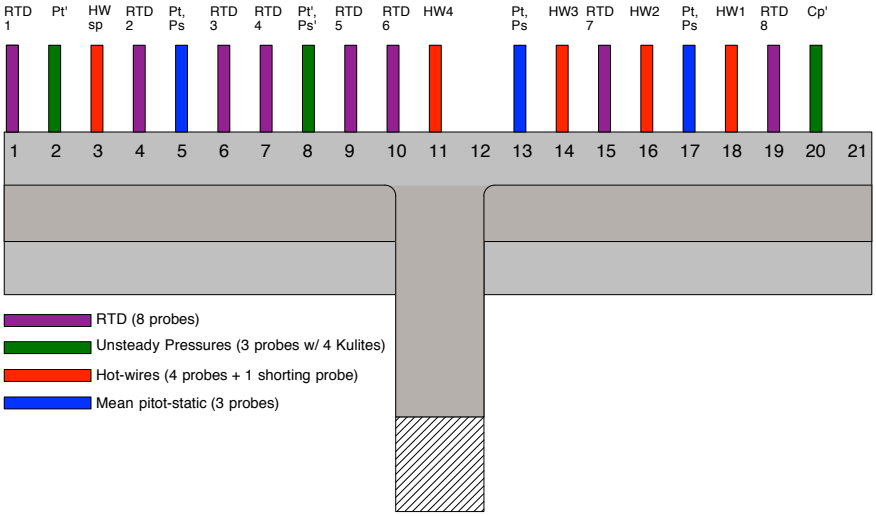

Figure 2: **Schematic depicting the probe layout in the 7-foot rake.**

limited to $q \approx 120$ MPa (2500 psf) due to frequent breakage of the hot-wire sensors at the large dynamic pressures.

The NTF survey rake, which spans 2.1 m (7 ft), was utilized as the test model. The rake is rated for cryogenic conditions and was mounted to the tunnel's model support structure. The rake has a chord length of 28.9 cm (11.375 in) and maximum thickness of 24 mm (0.952 in). It has sharp leading and trailing edges with included angles of 15° and a rectangular middle region. The rake has 21 ports for mounting probes that have a centerline-to-centerline spacing of 10.16 cm (4 in). A photograph of the rake populated with the test probes is shown in Fig. 1. Two long access covers that can be seen on the top of the rake are used to protect all of the electrical leads and pressure tubes in the access tray. All measurements were acquired with the rake fixed at a zero nominal angle of attack and at roll angles from $-180° < \phi < 180°$. The rake was populated with 19 probes and a sketch is shown in Fig. 2 showing the probe types and locations. All but two locations (12 & 21) have probes installed. The probe types include eight mean total temperature probes, three mean pitot-static probes, one fluctuating total pressure probe, one fluctuating static pressure probe, one combination fluctuating pitot-static probe, four hot-wire probes and one shorting probe. All the probes extended approximately 21.5 cm (8.45 in) ahead of the rake.

B. Measurement Probes and Instrumentation

The eight total temperatures at locations 1, 4, 6, 7, 9, 10, 15 and 19 (see Fig. 2) were measured with RTD class A sensors manufactured by Omega. The probe sheath diameters are 3.2 mm (1/8 in) with airflow holes in the sheath. The sensors are platinum type (Pt100) with a four-wire construction. All of the probes were calibrated post test for the range of temperatures tested and the test data reanalyzed using the updated coefficients. These measurements were acquired by the NTF's data acquisition system[17] (DAQ) at a sample rate of 50 Hz and sample period of 2 s. The three mean pitot-static probes at locations 5, 13 and 17 were also acquired with the NTF's data system. These probes have a diameter of 9 mm (0.356 in) and a cylindrical tip with an included angle of 10°. The static taps (4 equally spaced circumferentially) are 11.7 diameters downstream of the total pressure tap at the probe tip. These pressures were sampled at a rate of 10 Hz for 2 s.

Unsteady pressures were acquired with three probes. The fluctuating total pressure probe at location 2 is shown in Fig. 3a. A cryogenic-rated Kulite transducer (CCQ-062 series) with a diameter 1.7 mm (0.066 in) and a B screen installed was mounted at the tip of the probe. Similarly, Fig. 3b shows the fluctuating pitot-static probe at location 8 with the same type of pressure transducers at both the pitot and static tap locations. The static tap (not visible in the figure) points upward towards the ceiling when the rake is in the zero roll position and is approximately 10.7 diameters downstream of the pitot tap at the probe tip. A surface finish of 0.2 μm (8 μin) rms was prescribed for the pitot-static probe to prevent premature transition of the boundary layer on the probe. The static tap was designed to have a Helmholtz frequency ($>$ 20 kHz) well beyond our frequency of interest. Both the fluctuating total pressure and pitot-static probes were in-house designs implemented for this test. The transducers used in both probes are 172 KPa (25 psid) differential transducers with quoted resonant frequencies of approximately 240 kHz. For completeness, the

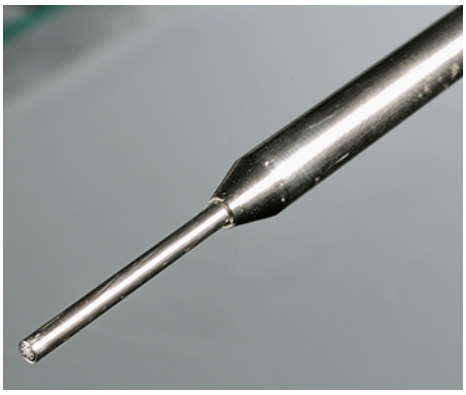

(a) Unsteady pitot probe

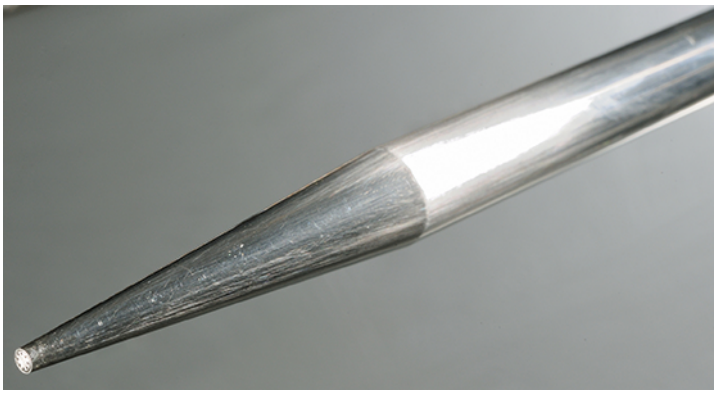

(b) Unsteady pitot-static probe

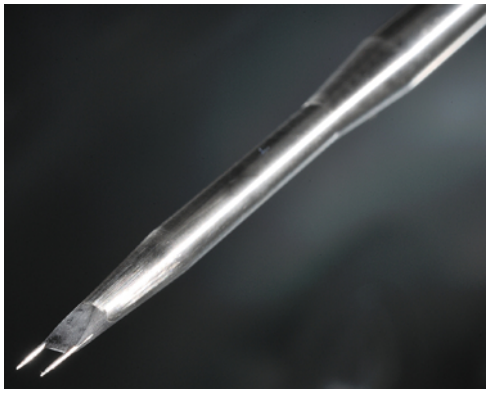

(c) Hot-wire probe

Figure 3: **Photographs of selected probes used for fluctuating measurements: (a) unsteady pitot probe @ loc 2; (b) unsteady pitot-static probe @ loc 8; (c) example hot-wire probe (locs 11, 14, 16 & 18).**

third unsteady pressure probe was a fluctuating static pressure probe (commercial probe not pictured) at location 20. Results from this probe will not be reported since the Helmholtz resonant frequency of 3 kHz was within our frequency of interest and as a consequence, it creates a bias in the data. An in-situ static calibration was applied to all the pressure transducers within a range of ±27.6 KPa (±4 psi). Excellent linearity and agreement versus the manufacturer's calibration was observed. The signal conditioning and excitation for the pressure transducers were provided by a quad bridge conditioner card. The conditioner card provides for each channel an AC/DC input coupler, pre- and post-gain amplifiers, and an 8-pole low-pass filter. All signals were AC coupled at 0.1 Hz and anti-alias filtered at 10 kHz. As with all of our unsteady measurements, we made a concerted effort to mitigate any extraneous line noise picked up by our sensors/instrumentation. We did not acquire mean pressures with these sensors.

Four single sensor hot-wire probes (see Fig. 3c) with the sensing element normal to the flow direction were installed at locations 11, 14, 16 and 18 . These probes were designed and built in house as integrated probes starting with commercially available sensor bodies. The integrated design was selected to prevent the probes from excessive vibrations or falling out of their supports at the severe cryogenic conditions as experienced in an earlier test. This design made it very cumbersome to replace the probes after a sensor damage so all sensor replacements were done in situ. The prongs were reinforced with epoxy to mitigate prong vibration. The sensors used were 5-μm platinum-plated tungsten with plated ends. The active sensor lengths are nominally 1.25 mm so that the length-to-diameter ratios are $l/d \approx 250$. A fifth hot-wire probe with an identical probe body and shorting sensor was located at location 3. This shorting probe was used to estimate the sensing element resistance as test temperature was changed since all the probes had the same cable lengths.

A TSI IFA-100 constant-temperature anemometer (CCA) was used for the portion of the test conducted at $T_t = 322$ and 172 K. The anemometer was operated in a 1:1 bridge configuration with an external arm to set the desired overheat ratios. Typical hot-wire frequency responses estimated with a square-wave test were approximately 180 kHz and 85 kHz for $T_t = 322$ K and 172 K, respectively. For the portion of the test at $T_t = 116$ K, we were unable to get a satisfactory square-wave response due in part to the changes in the cable inductances in the severe cryogenic environment. For these conditions, we used the AA Lab AN-1003 CCA system used by Wlezien et al.[14] with acceptable dynamic responses. Here we used a 1:1 internal bridge configuration. The estimated hot-wire frequency responses at $T_t = 116$ K were approximately 58 kHz. Similar to the unsteady pressures, the signal conditioning was done using 8-channel programmable filter/amplifier cards with similar characteristics to the card used for the pressure transducers except for the voltage excitation feature. Both mean and fluctuating measurements were acquired for the four hot-wire signals. For the mean component, we applied a low-pass filter of 30 Hz and unity gain to the DC coupled signal. For the fluctuating component, the signal was AC coupled at 0.1 Hz and low-pass filtered at 10 kHz.

The signals from the unsteady pressures and hot-wire sensors were acquired with a data system brought in for this test. As previously mentioned, all of the signal conditioning were done with the cards described earlier. The analog-to-digital conversion was done with two 8-channel 16-bit digitizer cards for all channels simultaneously. The number of samples acquired for each channel was typically 256000 samples at a sample rate of 25.6 kHz. The data were collected in a sequence where after getting to a test condition, the NTF DAQ system acquired data immediately followed by our DAQ system before going to the next test condition.

C. Measurement Reduction

1. Unsteady Pressures

The unsteady pressures presented are in the form of $\langle P'_s \rangle / q$ for the probe at location 8 and $\langle P'_t \rangle / q$ (or $\langle P'_t \rangle / \bar{P}_t$) for the probes at locations 2 and 8. If we look at the transfer functions $TF_{P'_t, P'_s}(f)$ between the signals at location 8, we see from the amplitudes that input/output relationships exist particularly for frequencies $f < 2$ kHz where most of the spectral energy resides. Considering the phase of the transfer function, a linear phase relationship is observed for those frequencies indicating a linear phase delay with slope $2\pi\tau_o$ where τ_o is the time delay related to the convection speed of the disturbances. Based on these results, it seems reasonable to compute fluctuating Mach numbers M' from the measured pressure field. It should be noted that the flow variables computed with the NTF DAQ system[17] do not assume perfect gas or constant specific heat ratio γ. For purposes of our small fluctuating analysis to follow, we make those assumptions. To validate our assumptions, the mean of our computed instantaneous values using these assumptions were compared to the values given by the NTF DAQ system assuming real gas and variable specific heat ratio.

The percent errors for our test conditions did not exceed 0.2%, 5.3%, and 2.8% for the Mach number, density, and velocity, respectively. With the maximum percent errors realized, the assumptions appear reasonable for the small fluctuating analysis. We start with the isentropic flow relations

$$\frac{P_s}{P_t} = \left(1 + \frac{\gamma - 1}{2} M^2\right)^{-\frac{\gamma}{\gamma - 1}} \tag{1}$$

where all flow variables represent instantaneous results and γ is assumed constant with a value of 1.4 for both air and nitrogen. If we rearrange and write all variables as mean and fluctuating components, the fluctuating Mach number then takes the form

$$\bar{M} + M' = \left\{ \frac{2}{\gamma - 1} \left[\left(\frac{\bar{P}_s + P'_s}{\bar{P}_t + P'_t} \right)^{-\frac{\gamma - 1}{\gamma}} - 1 \right] \right\}^{\frac{1}{2}} \tag{2}$$

where $\bar{P}_s$ and $\bar{P}_t$ were obtained from the tunnel conditions. We can then present this in the form of percent $\langle M' \rangle / \bar{M}$.

Continuing with this approach, we computed other unsteady flow variables derived from the acoustic field at location 8. The additional assumption made is small total temperature fluctuations ($\langle T'_t \rangle / \bar{T}_t \ll 1$). Total temperature fluctuations are generally small relative to turbulence levels in well designed wind tunnels; however some measurements in T2, which is an induction driven wind tunnel, were made that indicated large fluctuation levels of total temperature at cryogenic environment.[18] They reported levels of $\langle T'_t \rangle / \bar{T}_t \approx 1.4\%$ at $T_t = 100$ K. They note that most of the energy corresponds to low frequencies and attribute the large fluctuations to the temperature regulation process of spraying liquid nitrogen into the driving-air at room temperature. It should be noted that the operational procedures of T2 and NTF are very different where run times for T2 are typically 60 to 120 s. Since no direct measurements of the total temperature fluctuations were made in this test, we will continue with the generally accepted assumption of negligible T'_t levels. We begin by estimating the instantaneous density assuming perfect gas equation of state

$$\rho = \frac{P_s}{RT} \tag{3}$$

and again the isentropic flow relations

$$\frac{T}{T_t} = \left(1 + \frac{\gamma - 1}{2} M^2\right)^{-1} \tag{4}$$

where we assume $T_t \approx \bar{T}_t$. Combining Eqs. 1, 3, and 4, we get

$$\rho + \rho' = \frac{(P_s + P'_s)}{R\bar{T}_t} \left(\frac{P_s + P'_s}{P_t + P'_t} \right)^{-\frac{\gamma - 1}{\gamma}} . \tag{5}$$

Similarly, we solve for the instantaneous velocity using $u = Ma$ and applying the same assumptions to get

$$\bar{u} + u' = \left\{ \frac{2\gamma R\bar{T}_t}{\gamma - 1} \left[1 - \left(\frac{P_s + P'_s}{P_t + P'_t} \right)^{\frac{\gamma - 1}{\gamma}} \right] \right\}^{\frac{1}{2}} . \tag{6}$$

By combining Eqs. 5 and 6, we get an estimate for the acoustically derived massflux, $m = \rho u$, that can be compared to measurements obtained from hot-wire anemometry.

2. Hot Wires

Reduced hot-wire anemometry results are an essential part of this paper; however, there is no general consensus on how to reduce hot-wire results at transonic speeds. The hot-wire output is related to the non-dimensional heat loss, the Nusselt number Nu, that has been shown by Kovásznay[19] to have the functional form

$$Nu = Nu\left(M, Re, Pr, \tau, \eta, \frac{l}{d}\right) \tag{7}$$

where the recovery factor η and overheat ratio τ are defined as $\eta = T_e/T_t$ and $\tau = (T_w - T_e)/T_t$, respectively. For $l/d > 200$, the end-conduction effects are small and can be accounted for in the calibration so this dependence can be neglected. The Prandlt number Pr is typically assumed constant. In general, the recovery factor takes the form $\eta = \eta(M, Re)$, but for large wire Reynolds numbers ($Re_t > 20$), then $\eta \approx \eta(M)$.[20,21]

For low Mach number incompressible flows, $Nu \propto \sqrt{Re}$ (or $\sqrt{u}$) so the hot-wire calibration reduces to King's formula.[22] For flows with $M > 1.2$, the Nusselt number becomes independent of Mach number[23,24] and the calibration follows the process outlined by Smits et al.[25] where the wire responds to massflux ($m = \rho u$), τ and T_t. For transonic Mach numbers at large wire Reynolds numbers, the Nusselt number depends on M, Re, and τ and we are not in general able to isolate the dependence. Morkovin[23] has shown based on his hot-wire sensitivity analysis that the sensitivities to velocity and density are in general not equal in transonic flow. Some later works[26,27] suggest that at transonic speeds the hot-wire sensitivities to velocity and density are essentially equal ($S_u \approx S_\rho$) for large overheat ratios ($\tau > 0.4$) and $Re_t > 20$. Their results indicate that the wire responds primarily to massflux for a given overheat ratio and total temperature, i.e., acts as a massflux sensor. Rose and McDaid[26] do note however that many of their E versus m data were taken near sonic conditions. Rong et al.[28] conducted experiments for M ranging from 0.5 to 1.4, Re_t from 100 to 300 and τ from 0.8 to 1. They found that the hot-wire sensitivities to massflux and density are essentially equal ($S_m \approx S_\rho$) and use this to affirm the earlier findings;[26,27] however, they were unable to make direct measurements of S_u.

For the current study, hot-wire measurements were acquired for the three tunnel temperatures (322, 172 and 116 K) over a range of M and Re to determine if the primary response of the wire is to m or a combination of m and M. Special care was taken by the NTF staff to maintain the tunnel at near constant total temperature conditions (typically within ± 1 K). We measured the hot-wire response for a range of m at constant M (or u) and in some instances at constant ρ. The wire Reynolds numbers were $20 < Re_t < 900$ and the wire overheat ratios were $0.7 < \tau < 1.5$, assuming a recovery factor of $\eta = 0.99$. All calibration data were acquired with the rake in the nominal zero roll position ($\phi = 0°$). Calibration data in the form of E vs m were plotted for the range of Mach numbers ($0.2 \leq M_a \leq 0.95$) tested using the freestream massflux for the calibration. An example plot for an air-mode condition is shown in Fig. 4. All of the data shown were acquired with one hot-wire sensor located at rake location 16 (HW2). The tunnel temperature and overheat ratio were held constant for all the data points shown ($T_t = 322$ K and $\tau = 0.7$). The plot clearly demonstrates that the output depends on both massflux and Mach number, i.e., $E = E(\rho u, M)$ and questions the validity of the velocity and density sensitivities being approximately equal ($S_u \approx S_\rho$). The anemometer output reduces with increasing Mach number. This dependency was observed for all the temperatures tested and for overheat values as large as $\tau = 1.5$. For each Mach number in the figure, calibration curves were computed using the expression below

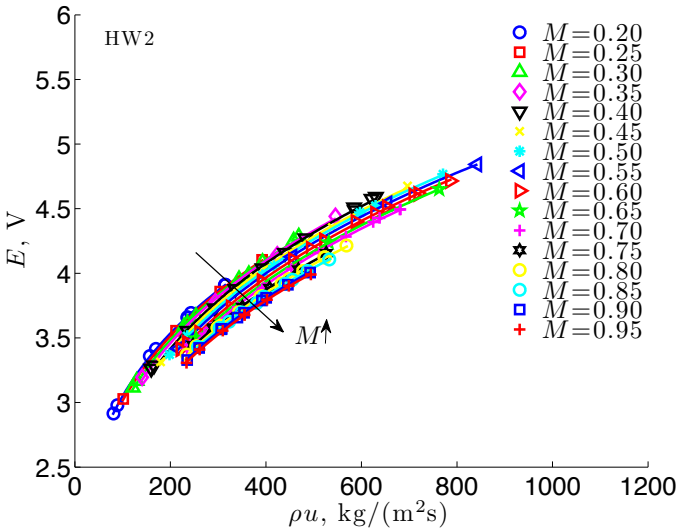

Figure 4: Hot-wire voltage output versus massflux for a range of Mach numbers. Data shown are for air-mode runs at $T_t = 322$ K.

$$E^2 = A + B \cdot (\rho u)^n \tag{8}$$

where $E^2 = E_o^2 \cdot (T_t/T_C)$ and A, B and n are the calibration constants. E_o is the output bridge voltage, T_t is the measured RTD total temperature adjacent to the probe, and T_C is the mean calibration temperature of all the calibration points for the selected probe. For all the calibrations in this study, we found that a value of $n = 0.5$ for the exponent was satisfactory. The temperature correction to the anemometer bridge output is done to account for variations in T_t relative to T_C.

As part of the test matrix, we acquired data for a range of ρ values while holding constant M (or u), T_t, and τ. We applied a calibration fit similar to Eq. 8 where $E^2 \propto \rho^n$ instead of $E^2 \propto (\rho u)^n$. The sensitivities to density are computed by applying $S_\rho = \frac{\rho}{E}\frac{\partial E}{\partial \rho}$ to the calibration curve. Similarly, data were acquired for a range of u values while holding ρ, T_t, and τ constant and again applying a calibration akin to Eq. 8, $E^2 \propto u^n$. The sensitivities to velocity were then computed using $S_u = \frac{u}{E}\frac{\partial E}{\partial u}$. Both sets of calibration curves fit the experimental data very well. The resulting sensitivities for the data shown in Fig. 4 are presented in Fig. 5 and this confirms the assertion of $S_u \neq S_\rho$ for our test conditions. If we reconsider Fig. 4, we see that the output voltage is $E = E(m, M)$ and for small fluctuations the fluctuating output can be written as

$$\frac{E'}{\bar{E}} \approx S_m \cdot \left(\frac{m'}{\bar{m}} + \frac{S_M}{S_m}\frac{M'}{\bar{M}} \right) \qquad (9)$$

provided that T_t and τ are constant. If $|S_M/S_m| \ll 1$ and the relative fluctuation levels for m and M are of the same order of magnitude, then we can assume that the wire responds primarily to massflux. The next logical step is to estimate the sensitivities to both m and M. The sensitivities to massflux, S_m, follows as before by directly applying Eq. 8 for each M. The sensitivities to Mach number were obtained by making use of the calibration curves obtained at a constant Mach number ($E = E|_M(\rho u)$). Several constant massflux values were selected and the E values were evaluated for each M using Eq. 8. The composite plot for all the Mach number and selected massflux values are shown in Fig. 6. Fourth-order polynomial curve fits were applied to the data for each massflux and the sensitivities were computed using $S_M = \frac{M}{E}\frac{\partial E}{\partial M}$. The resulting sensitivities, S_m and S_M, are shown Fig. 7. These values suggest that $|S_M/S_m| \ll 1$ for small and large values of M for our range of Mach numbers.

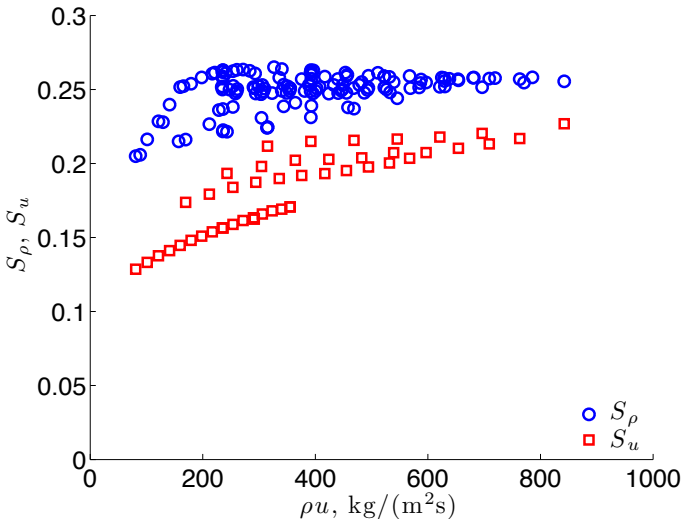

Figure 5: Hot-wire sensitivities to velocity and density for a range of massflux over a range of $0.2 \leq M \leq 0.95$. Data shown are for air-mode runs at $T_t = 322$ K.

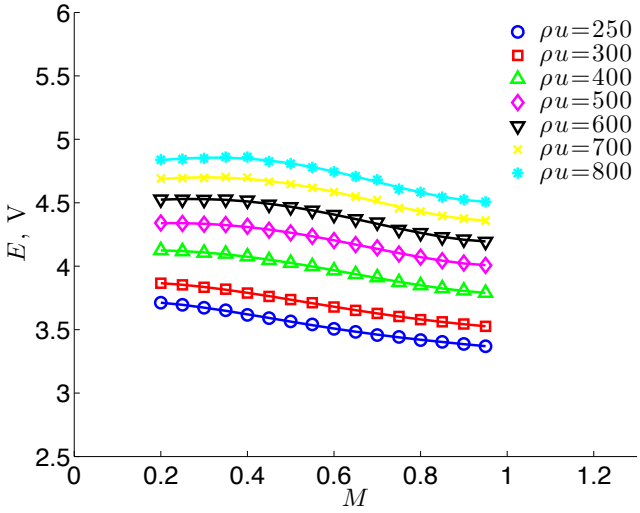

Figure 6: Interpolated hot-wire output for a range of constant massflux values over a range of $0.2 \leq M \leq 0.95$. Data shown are for air-mode runs at $T_t = 322$ K.

For the range of Mach numbers evaluated in this study, we found that the hot-wire responses were predominantly sensitive to massflux for Mach number ranges of $0.2 \leq M \leq 0.5$ and $0.85 \leq M \leq 0.95$. Recall that these findings are for large wire Reynolds number, $Re_t > 20$, and large overheat ratios, $\tau > 0.7$. Example calibration plots that represent all the temperatures tested are shown in Fig. 8. The data collapse of E versus ρu for the Mach number range, $0.2 \leq M \leq 0.5$, is very good as demonstrated in Figs. 8a and 8b. Similarly, the data presented in Figs. 8c and 8d for $0.85 \leq M \leq 0.95$ show similar trends. The mean temperature and the two standard-deviation values shown in the plots are the computed values for the measured tunnel stagnation temperatures during the calibration runs. The $2\sigma_{T_t}$ values are typically less than 2 K which is evidence of how stable we were able to maintain tunnel temperatures. The total temperatures used in Eq. 8 to correct the measured output voltage E_o are the temperatures measured with

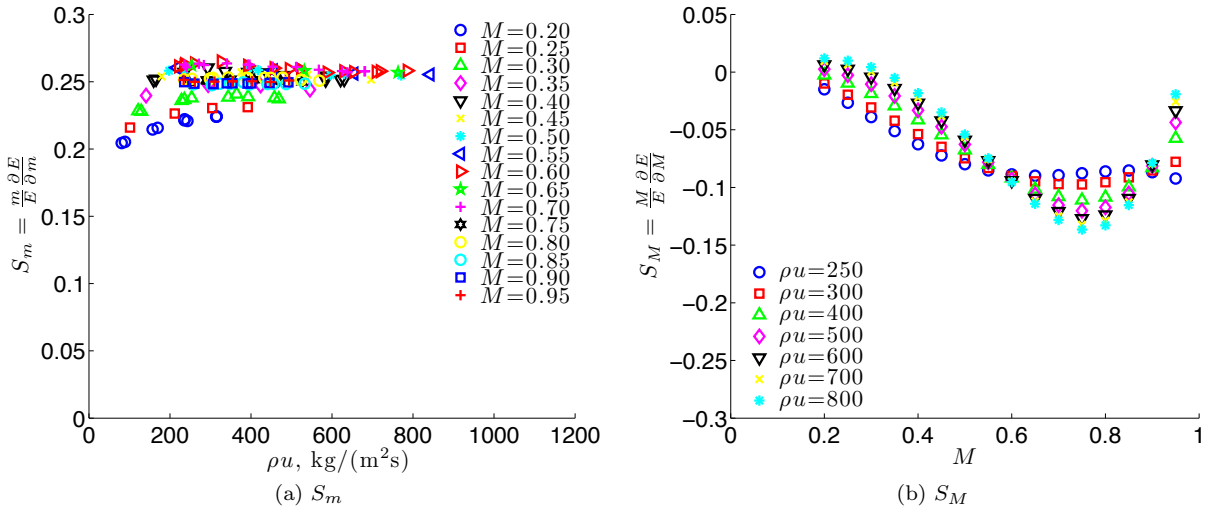

(a) S_m (b) S_M

Figure 7: Hot-wire sensitivities to (a) massflux and (b) Mach number for a range of massflux and Mach numbers. Data shown are for air-mode runs at $T_t = 322$ K.

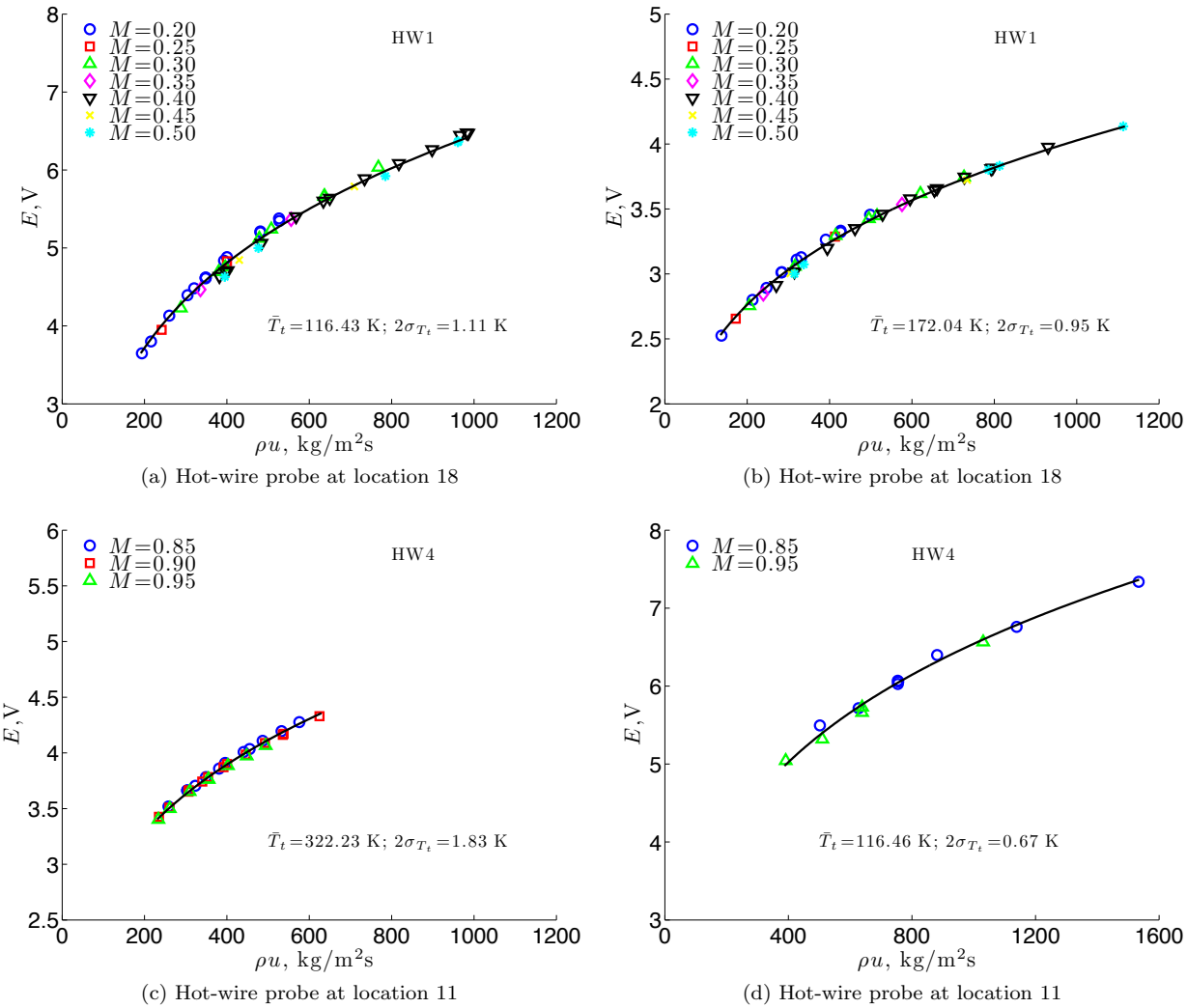

(a) Hot-wire probe at location 18 (b) Hot-wire probe at location 18

(c) Hot-wire probe at location 11 (d) Hot-wire probe at location 11

Figure 8: Examples of hot-wire calibration at (a) T_t = 116 K and (b) T_t = 172 K for $0.2 \leq M \leq 0.5$ and at (c) $T_t = 322$ K and (d) $T_t = 116$ K for $0.85 \leq M \leq 0.95$.

the RTD probes closest to the hot-wire probes to account for any spatial total temperature variations. For the four hot-wire probes used, RTD8 was used for HW1, RTD7 for HW2 & HW3, and RTD6 for HW4 (see Fig. 2). Using the measured voltages, Eq. 8 is solved for the massflux

$$\rho u = \left(\frac{E^2 - A}{B} \right)^{1/n}. \tag{10}$$

Since it is not possible to separate the dependence between M and ρu of the wire response with a single wire and overheat ratio, no attempt is made here to reduce the hot-wire data for Mach numbers in the range $0.55 \leq M \leq 0.8$.

III. Results

The results are to be presented first for the unsteady pressures followed by the hot-wire measurements. As stated previously, the number of samples acquired for each channel was typically 256000 samples at a sample rate of 25.6 kHz. Unless otherwise stated, all unsteady measurements were acquired for a frequency bandwidth of 0.1 Hz $\leq f \leq$ 10 kHz. Hanning data windows are applied to the computed power spectral densities with 50% window overlapping and a resulting frequency resolution of 10 Hz. The rms of the fluctuating values presented are computed over the entire frequency bandwidth. The frequency range recommended by the NWTC[29] to remove ambiguity in reporting is 1 Hz $\leq f \leq$ 100 kHz, which is not the same as reported here. We include lower frequencies in our analysis and do not extend to the larger frequencies where our energy content is very low (power spectral densities will be presented later).

In the following sections, the data are examined for the rake in the nominal zero roll position, $\phi = 0°$, followed by roll polar surveys. Fig. 2 shows a top-down view from the ceiling perspective of the rake in the nominal zero position. The roll polar data were acquired starting at $\phi = -180°$ to 180° in increments of 6°. Looking upstream towards the flow direction, positive ϕ is clockwise following the right hand rule. When viewing roll polar plots, $\phi = -90°$ and 90° correspond to the tunnel ceiling and floor, respectively, and $\phi = 0°$ and $\pm 180°$ represent the inner and outer sidewalls. So for example, the rake is positioned at $\phi \approx -45°$ in the photograph shown in Fig. 1. As pointed out earlier, the main motivation for using the survey rake is to measure the spatial distribution of the disturbance field in the test section. The NTF has a cooling coil and associated support structure that is utilized only for air-mode testing. An isometric view of the rapid diffuser section with the support structure (not cooling coil) is shown in Fig. 9a. The support structure is sometimes referred to as the wagon wheel for obvious reasons. The radii of the outer and inner rings that support the spokes of the wagon wheel structure are approximately 4.1 m (13.4 ft) and 1.2 m (4 ft), respectively, with nominal spoke spacings of 22.5°. The cooling coil is attached to the downstream end of the wagon wheel and just upstream of the four turbulence treatment screens in the settling chamber. A photograph showing a downstream view of the cooling coil and wagon wheel is shown in Fig. 9b. The wagon wheel support structure does not extend through the cooling coil so it is not visible on the downstream side of the cooling cool. The vertical and horizontal plates, which join the separate cooling coil sections, extend through the coil. The short horizontal plates have streamlined trailing edges but the long vertical plates have blunt trailing edges. Both the wagon wheel support structure and the cooling coil arrangement are potential sources of wakes and/or shear layers that can have adverse effects on the test-section disturbance field.

A. Pressure Results

Selected unsteady pressures for the rake located at $\phi = 0°$ are presented first. The unsteady static pressures measured at location 8 are presented in Fig. 10a and are normalized by the dynamic pressure q. Recall that in this configuration, the static tap on this probe points towards the tunnel ceiling. The NWTC reports[29,30] provide recommended guidelines of flow quality requirements for transonic wind tunnels. For the static pressure fluctuations, the recommended threshold values for $\langle P_s' \rangle / q$ are 0.3 and 0.6% at Mach numbers of 0.3 and 0.8, respectively. These recommended levels as well as predicted trends from the report[30] are included in the figure. These results compare favorably with past measurements reported for NTF[13,14] and for ETW.[5] A similar plot is shown in Fig. 10b for the unsteady total pressures $\langle P_t' \rangle / \bar{P}_t$ measured at location 2 except that these are normalized by the tunnel total pressures (not shown–data for location 8 very similar). The similarity between the data for warm and cryogenic conditions is noteworthy where there is a subtle

performance benefit at the air conditions ($T_t = 322$ K). The expected peak in the fluctuations occur around $M = 0.8$. The measured values are comparable to the recommendations given by NWTC except for the large variations of $\langle P'_s \rangle / q$ for low Mach numbers ($M \leq 0.4$). The large values for the cryogenic modes at $M = 0.2$ are significant. These variations are more evident in the data of Fig. 10b if normalized by q instead of $\bar{P}_t$. The data plotted versus Reynolds number (not shown here) suggest that it is not simply a Reynolds number effect of the probes. Similar statistical variations in unsteady pressures at these Mach numbers have

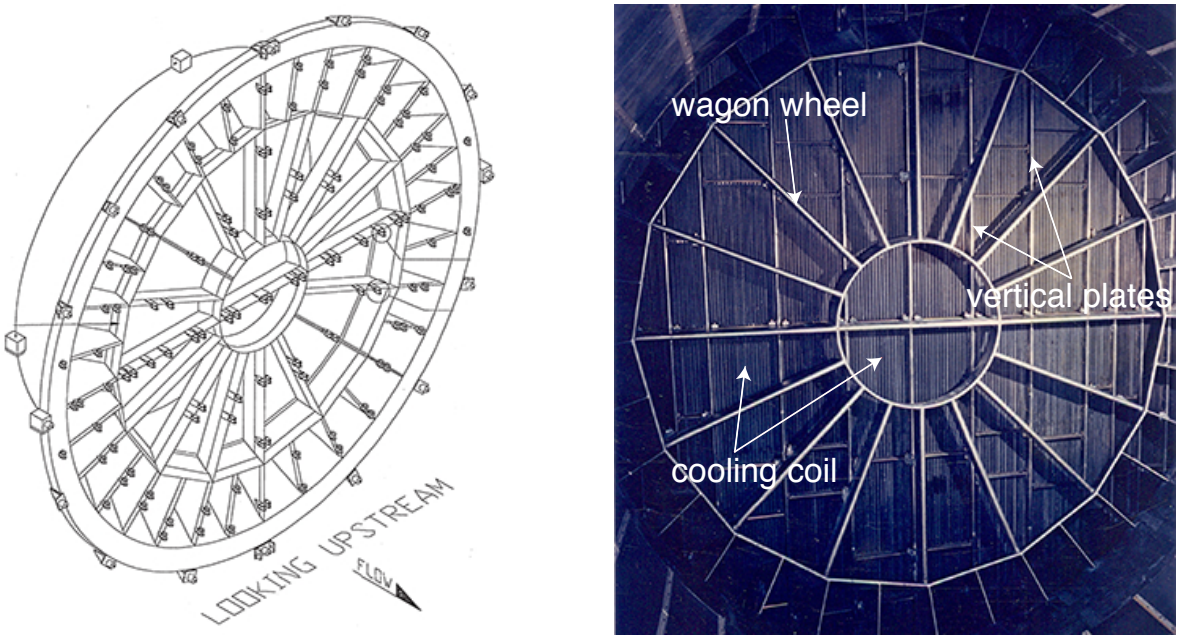

(a) Isometric view of rapid diffuser

(b) Downstream view of wagon wheel/cooler assembly

Figure 9: Possible sources of unsteady disturbances depicted in (a) an isometric view of the support structure (wagon wheel) and (b) a photograph of the cooling coil and associated support structure.

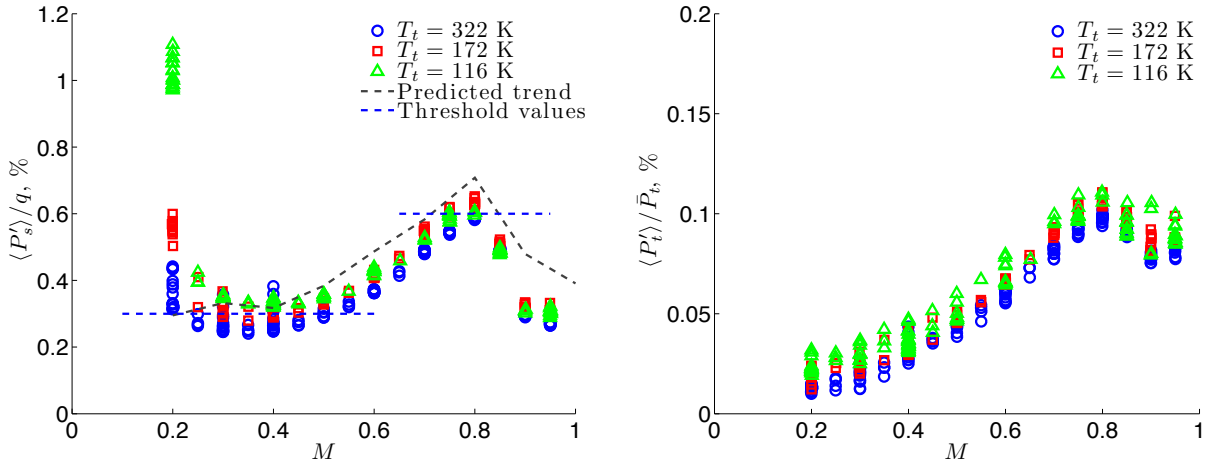

(a) Static pressure probe @ location 8

(b) Total pressure probe @ location 2

Figure 10: Plots of normalized unsteady pressures, (a) static and (b) total, versus Mach number at the three tunnel temperatures for $\phi = 0$. NWTC recommended threshold values[29] for M = 0.3 and 0.8 and a predicted trend[30] of fluctuating static pressure versus Mach are included.

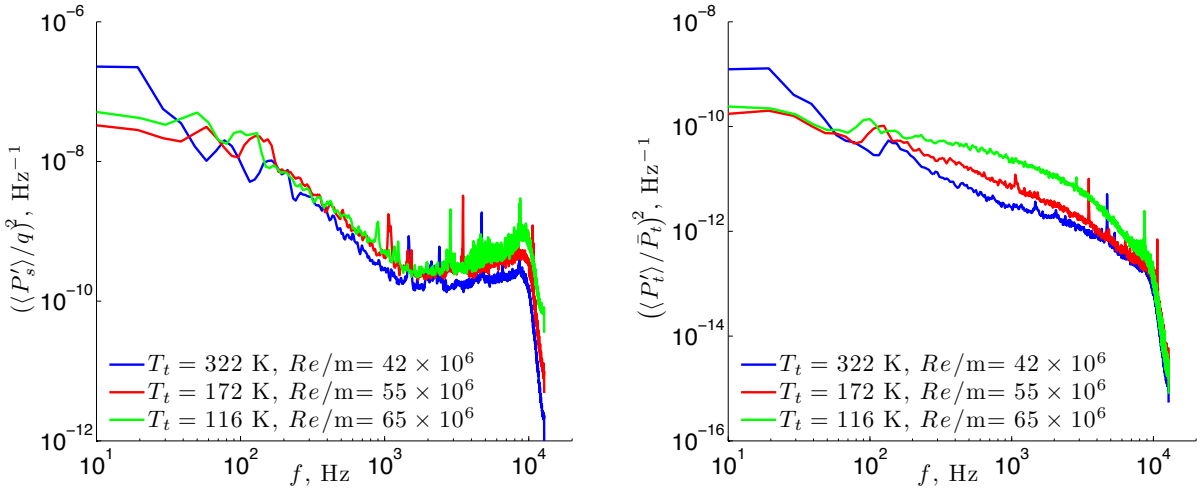

(a) Static pressure probe @ location 8

(b) Total pressure probe @ location 2

Figure 11: **Selected power spectral densities at M = 0.3 for data presented in Fig. 10 in the form of (a) $\langle \mathbf{P_s'} \rangle / \mathbf{q}$ and (b) $\langle \mathbf{P_t'} \rangle / \bar{\mathbf{P}}_\mathbf{t}$.**

been observed in the past[31,32] using unsteady pressure transducers mounted on the tunnel sidewalls. They reported that this behavior is believed to be related to the dynamics of the model support structure and load path. Representative PSD's for the three temperatures at $M = 0.3$ are shown in Fig. 11. The $\langle P_s' \rangle / q$ spectral energies in Fig. 11a are similar in shape except for the low frequencies ($f < 30$ Hz) in the air mode. Most of the spectral energy resides at frequencies below a couple hundred Hertz. However, for the $\langle P_t' \rangle / \bar{P}_t$ in Fig. 11b, the spectrum becomes fuller as the temperature decreases. The air-mode PSD again shows more energy at the low frequencies.

For the flow variables derived from the acoustic measurements in the data to follow, we need to keep in mind that the data for Mach numbers less than 0.4 may not accurately represent the flow variables due to the large statistical variations in the measured unsteady pressure field. The fluctuating Mach number and density derived from the acoustic measurements are computed using Eqs. 2 and 5 and the results are depicted in Fig. 12. We do not believe the large fluctuations in $\langle M' \rangle / \bar{M}$ for Mach numbers less than 0.4 are real. Values of $\langle M' \rangle / \bar{M}$ for air are approximately 0.13% at $M = 0.4$ with maximum values $\langle M' \rangle / \bar{M} \approx 0.35\%$ at $M = 0.8$. The levels of the density fluctuations shown in Figs. 12b are significantly lower than those for the Mach number fluctuations (recall that T_t' is assumed negligibly small here). As is no surprise, the incompressible values of $\langle \rho' \rangle / \bar{\rho}$ are an order of magnitude lower than for the larger Mach values. Similarly, we compute the velocity ($\langle u' \rangle$) and massflux ($\langle m' \rangle$) fluctuations using Eqs. 5 and 6. These are presented in Figs. 13. The values of $\langle u' \rangle / \bar{u}$ at $M = 0.4$ are approximately 0.12% for air and 0.20% for the coldest cryogenic condition with maximum values of about 0.32% at $M = 0.8$. The corresponding massflux values in Figs. 13b show similar trends where again the air-mode data show more favorable fluctuation levels. As a side note, the relative fluctuation levels of Mach number and massflux derived from the acoustic measurements are on the same order of magnitude, $\sim 0.1\%$, and consequently, M' should not in general be simply neglected in the hot-wire analysis. However, referring back to Eq. 9, recall that neglecting the M' contributions is acceptable only when $|S_M / S_m|$ is small.

To explore the spatial distribution of the unsteady pressures, we examine the variation of the rms fluctuating pressures as a function of roll angle. Recall that the three unsteady pressure sensors are at locations 2 and 8, which are at a radii of $r = 91.4$ cm (36 in) and 30.5 cm (12 in), respectively, from the center of rotation of the rake. Fig. 14 shows plots of $\langle P' \rangle / q$ versus ϕ for two conditions at $M = 0.2$. For the air-mode condition in Fig. 14a, the fluctuating pressures P_t' at location 2 show significant variations at $\phi \approx 0$, ± 90 and $\pm 180°$ with the largest occurring when the rake is positioned vertically ($\phi \approx \pm 90°$). These large variations are a factor of two larger than the baseline values of $\langle P_t' \rangle / q \approx 0.4\%$. The variations in P_t' at location 8 do not exhibit similar excursions. The P_s' at location 8 is relatively insensitive to the roll angle and this trend is seen throughout the data for all Mach numbers. This insensitivity to roll angle was also evident for the

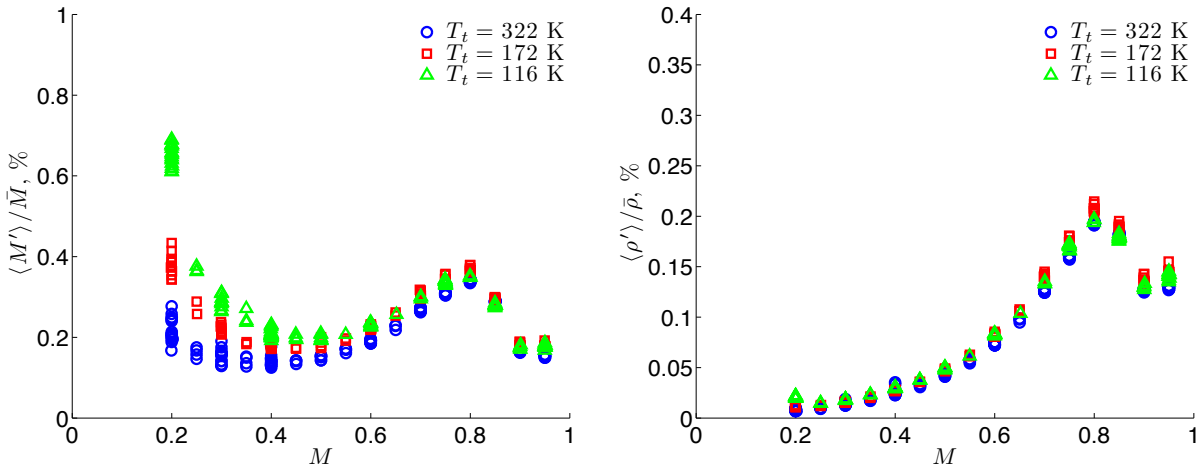

(a) Fluctuating Mach number

(b) Fluctuating density

Figure 12: **Plots of normalized fluctuating (a) Mach number and (b) density (derived from pressure field) versus Mach number at the three tunnel temperatures for $\phi = 0$.**

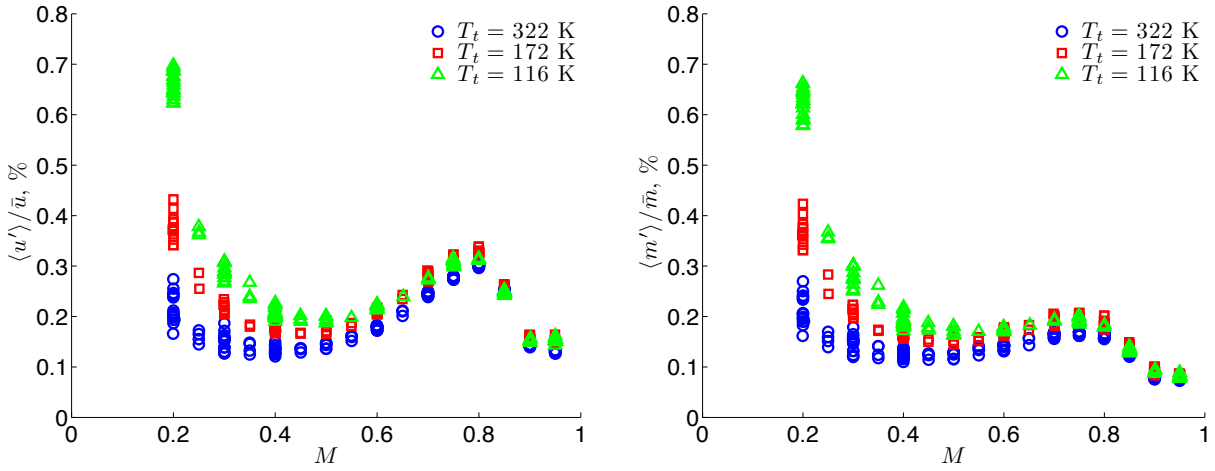

(a) Fluctuating velocity

(b) Fluctuating massflux

Figure 13: **Plots of normalized fluctuating (a) velocity and (b) massflux (derived from pressure field) versus Mach number at the three tunnel temperatures for $\phi = 0$.**

more outboard static probe at location 20 ($r = 91.4$ cm, data not shown) so the insensitivity of the unsteady static pressures to roll angle is most likely not just due to radial location. Another $M = 0.2$ condition at a larger unit Re in the cryogenic mode is shown in Fig. 14b. As is expected from the earlier plots (see for example Fig. 10), the baseline values of all the measurements are considerably larger than the corresponding values in the air mode. The excursions in P_t' at location 2 at $\phi \approx \pm 90$ are about 15% of the baseline value, significantly less than for the air mode. Also, there are some variations in P_t' at location 8, more than observed for the air mode. These excursions do not correspond to the same roll angles as for P_t' at location 2 and are only observed in the roll polar data acquired at $M = 0.2$. Next we consider data for $M = 0.4$ and these are presented in Fig. 15. The flow disturbances P_t' at location 2 for $\phi \approx \pm 90$ are still clearly evident, though their levels are diminished especially for the higher Re cryogenic condition in Fig. 15b. Note that the other measured unsteady pressure disturbances are fairly spatially homogeneous with roll position. Similar data for $M = 0.85$ are presented in Fig. 16 over a range of Reynolds number for both air and cryogenic conditions.

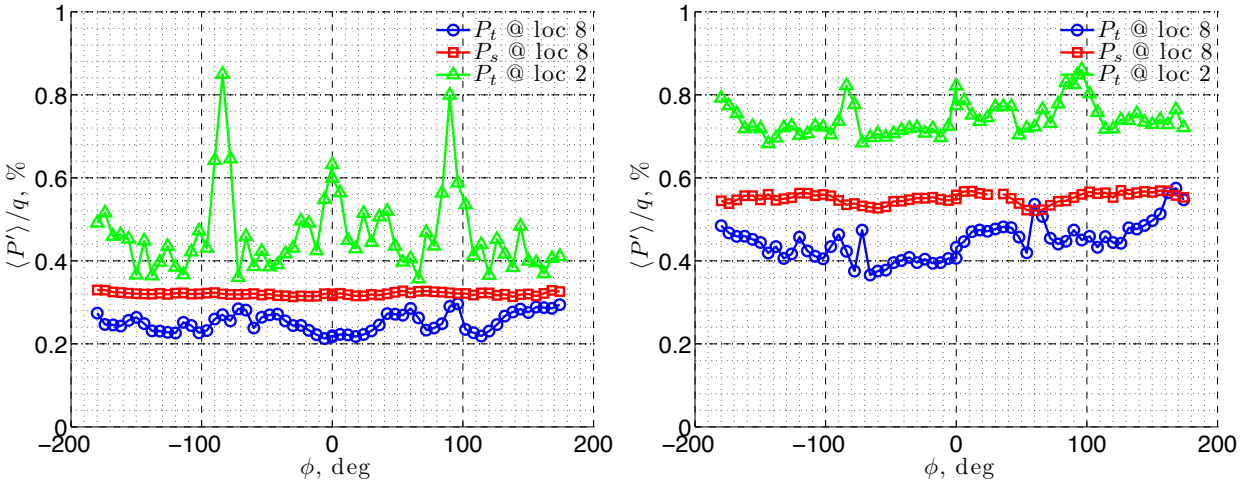

(a) Air mode, $Re/\text{m} = 16.3 \times 10^6$ (b) Cryogenic mode, $Re/\text{m} = 37.6 \times 10^6$

Figure 14: Spatial distribution of fluctuating pressures at M = 0.2 for (a) T_t = 322 K and (b) T_t = 172 K.

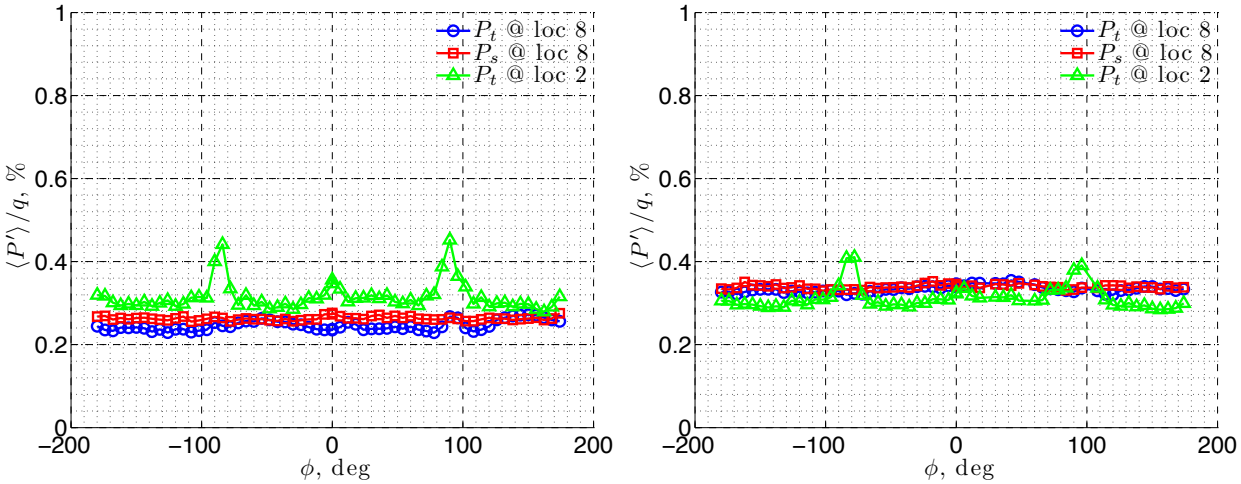

(a) Air mode, $Re/\text{m} = 30.9 \times 10^6$ (b) Cryogenic mode, $Re/\text{m} = 104.5 \times 10^6$

Figure 15: Spatial distribution of fluctuating pressures at M = 0.4 for (a) T_t = 322 K and (b) T_t = 116 K.

Some general observations can be made with respect to the spatial distribution of the acoustic disturbances in the NTF test section. The unsteady pressure disturbances measured at location 8 (P'_s & P'_t) are in general insensitive to roll angle except for the data acquired at $M = 0.2$ (possible structural vibration effect). Outboard variations in the unsteady disturbances (measured with a probe located at a radial distance of 0.91 m) were measured at discrete locations, but the disturbances were otherwise homogenous with respect to ϕ. For $M \geq 0.4$, the discrete locations are $\phi \approx \pm 90°$ (rake positioned vertically) and $\phi \approx 0$ and $\pm 180°$ (rake positioned horizontally). The data clearly demonstrate a unit Reynolds number effect on the level of the excursions with respect to the baseline values and possibly a Mach number effect. The excursion levels decrease with increasing unit Re and M. The excursions that exist when the rake is positioned horizontally are diminished to almost undetectable levels for the $M \geq 0.6$ and/or $Re/m \geq 100 \times 10^6$. However, the excursions at $\phi \approx \pm 90°$ never reach undetectable levels, though they remain relatively small, and can be seen for Mach and Reynolds numbers as large as $M = 0.95$ and $Re/m = 191 \times 10^6$.

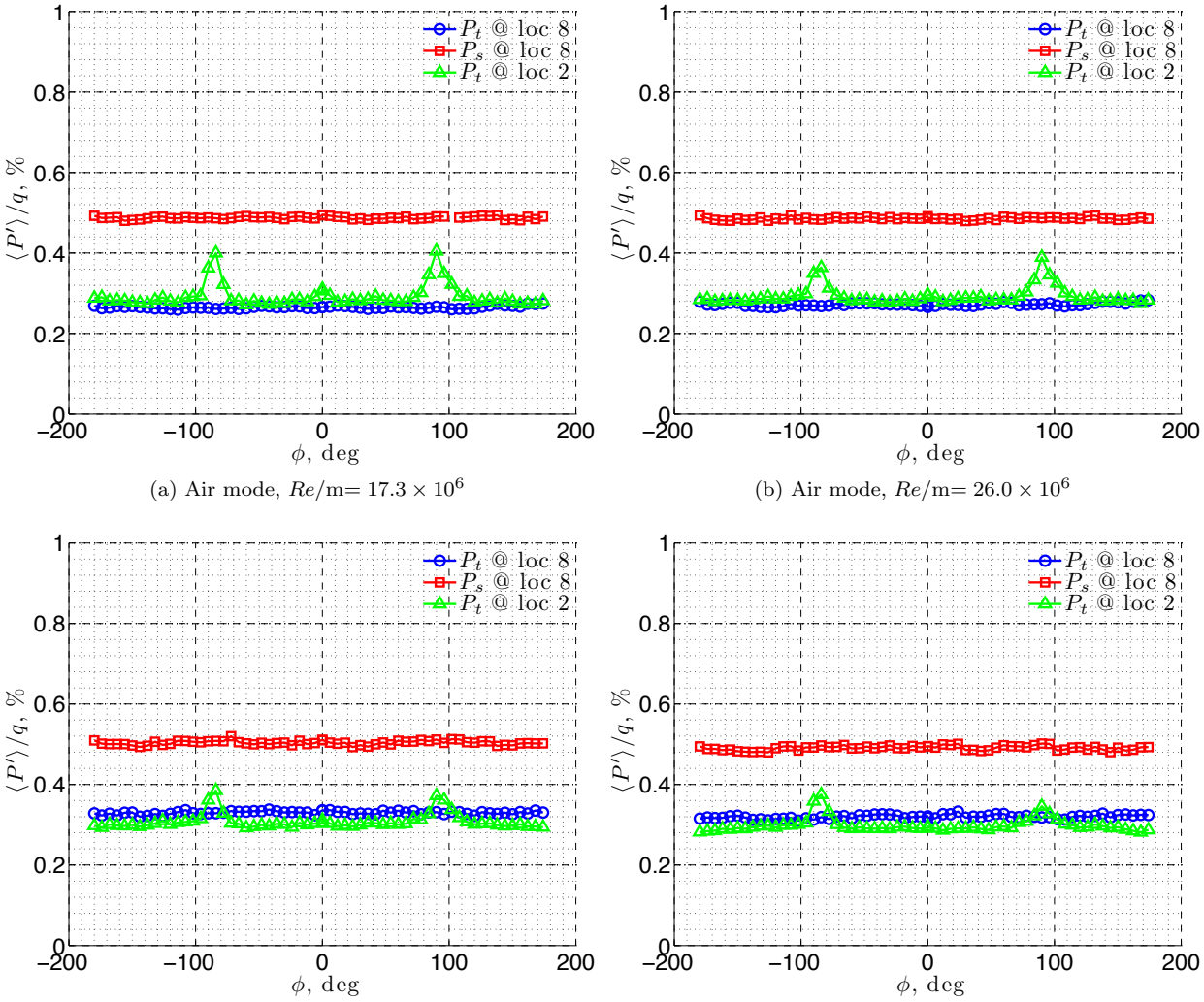

(a) Air mode, $Re/\mathrm{m} = 17.3 \times 10^6$

(b) Air mode, $Re/\mathrm{m} = 26.0 \times 10^6$

(c) Cryogenic mode, $Re/\mathrm{m} = 82.0 \times 10^6$

(d) Cryogenic mode, $Re/\mathrm{m} = 108.6 \times 10^6$

Figure 16: Spatial distribution of fluctuating pressures at M = 0.85 for (a) T_t = 322 K, (b) T_t = 322 K, (c) T_t = 172 K, and (d) T_t = 116 K.

B. Hot-Wire Results

The hot-wire data will first be presented for the nominal rake position followed by the roll polar data. Recall from the discussion in Section II.C.2 that the hot-wire output was shown to be predominantly sensitive to massflux, $m = \rho u$, for Mach numbers in the range $0.2 \leq M \leq 0.5$ and $0.85 \leq M \leq 0.95$. The results to be presented are only for these Mach number ranges. Massflux intensity data, $\langle m' \rangle / \bar{m}$, with the rake positioned at $\phi = 0$ are presented in Fig. 17. Included in the figures, just as a reference, are the NWTC[29] recommended value of turbulence intensity ($\langle u' \rangle / \bar{u} = 0.07\%$) that are inferred from low-speed ($M < 0.4$) measurements. Note that for incompressible Mach numbers, $\langle u' \rangle / \bar{u} \approx \langle m' \rangle / \bar{m}$ since $\langle \rho' \rangle / \bar{\rho}$ is negligibly small for these conditions (see Fig. 12b). The data shown are for selected probes and represent all the points used for the given hot-wire calibrations. The air-mode data in Fig. 17a were acquired using two different sensors for HW2 at location 16. We limited the overheat ratios to $\tau \approx 0.75$ to avoid driving the sensor temperatures too high ($T_w < 300^\circ$ C). A careful examination of the air data shows that for $M < 0.5$, the $\langle m' / \bar{m} \rangle$ values are generally less than 0.2% for most of the data. The intensity values for the high Mach number data are approximately 0.3%. A few intensity levels for $M \leq 0.45$ and $Re/\mathrm{m} < 12 \times 10^6$ fall within the NWTC recommendations. The larger intensity levels at $0.3 \leq M \leq 0.5$ are partly due to increased low-frequency fluctuations and some broadband energy increase (more on this later). The next two plots,

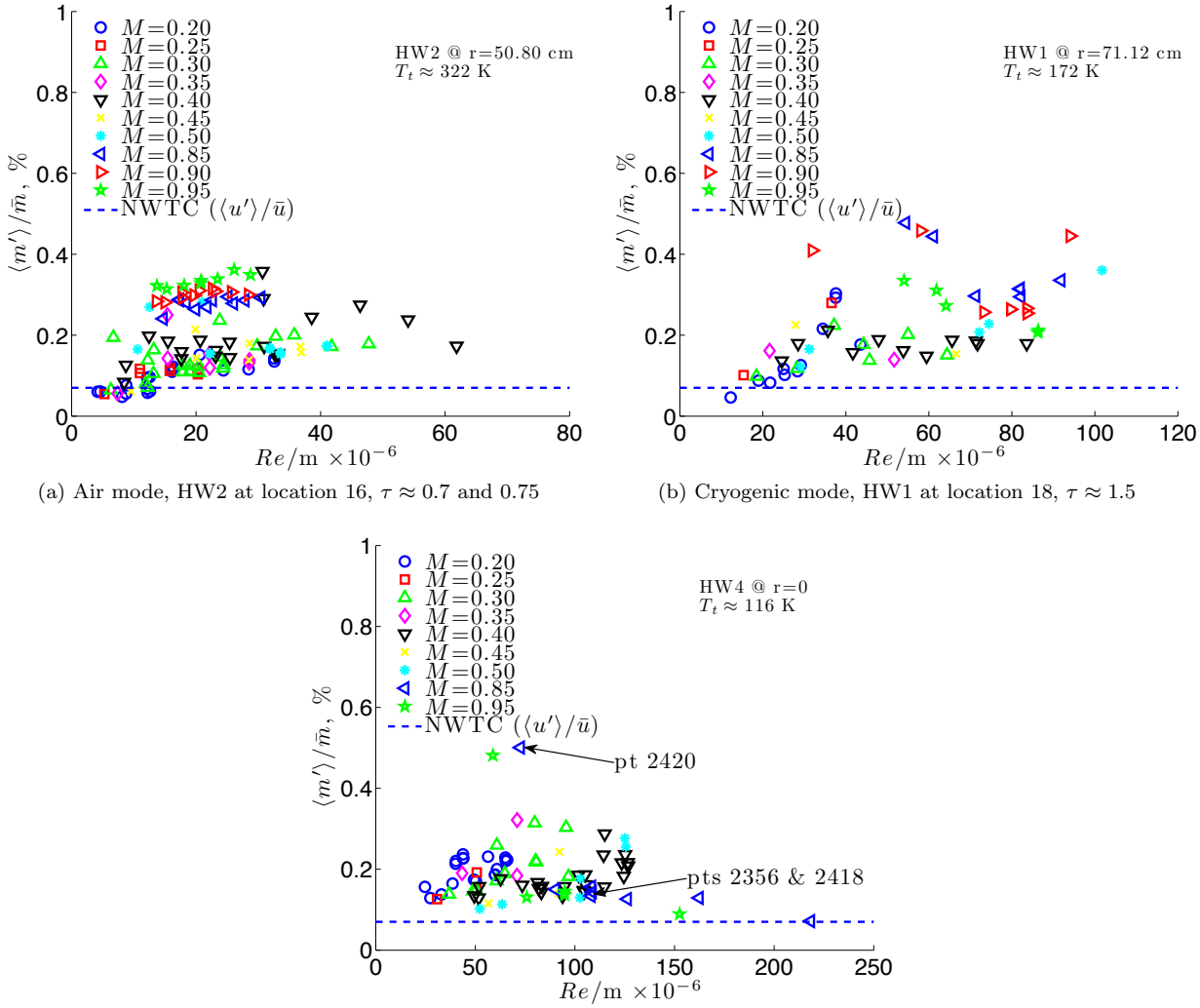

(a) Air mode, HW2 at location 16, $\tau \approx 0.7$ and 0.75

(b) Cryogenic mode, HW1 at location 18, $\tau \approx 1.5$

(c) Cryogenic mode, HW4 at location 11, $\tau \approx 1.5$

Figure 17: Percent massflux fluctuating intensities as a function of Reynolds number and Mach number for (a) $T_t = 322$ K , (b) $T_t = 172$ K, and (a) $T_t = 116$ K. Data at the nominal rake location, $\phi = 0$.

Figs. 17b and 17c, show similar data at different locations for the two cryogenic conditions corresponding to larger Reynolds numbers. The data in Fig. 17b were acquired with one sensor that survived the test matrix, meanwhile the data presented in Fig. 17c were acquired with three sensors. Similar intensity values are observed for $0.2 \leq M \leq 0.5$ with the levels of $\langle m' \rangle / \bar{m}$ on the order of 0.2%. For the larger Mach number range, the intensities for the air-mode and first cryogenic-mode measurements (Figs. 17a and 17b) have fairly consistent levels of $\langle m' \rangle / \bar{m} \sim 0.3\%$ except for a few larger values at the cryogenic condition for Mach 0.85 and 0.9. The cryogenic data at $T_t \approx 172$ K suggest lower $\langle m' \rangle / \bar{m}$ levels in the range of approximately $60 \times 10^6 < Re/\text{m} < 90 \times 10^6$. The lowest cryogenic-temperature condition (Fig. 17c) show much lower intensity levels of $\langle m' \rangle / \bar{m} \sim 0.1\%$ for $Re/\text{m} > 75 \times 10^6$ at the large transonic Mach numbers. The $\langle m' \rangle / \bar{m}$ measured with the hot-wire are somewhat larger than (except at the very low Mach numbers) the corresponding values inferred from the acoustic measurements (see Figs. 13b).

Previous $\langle u' \rangle / \bar{u}$ data acquired by McGinley et al.[13] in the NTF compared with three other large NASA facilities (8-Ft TPT, LTPT and Ames 11 Foot) are shown in Figs. 18. The NTF data were acquired in two separate tunnel entries, 1999 and 2000, and are denoted by black and red symbols, respectively. The NTF, LTPT and 8-FT TPT were high-passed at 0.1 Hz and the Ames data at 1 Hz. The NTF data were

acquired for $0.2 \leq M \leq 0.4$ and for Reynolds numbers limited to $Re/\text{m} \approx 50 \times 10^6$ ($Re/\text{ft} \approx 15 \times 10^6$) using a side mounted strut on each side wall. The intensity levels are in general consistent with the current findings. The turbulence intensity levels tend to increase with Mach number at a given Reynolds number. Also, for low Reynolds number ($Re/\text{m} < 15 \times 10^6$), the $\langle u' \rangle / \bar{u}$ levels approach the NWTC recommended level at the lower Mach numbers. The figure also includes the $\%Tu$ requirement recommended by Boeing circa 1999, $\langle u' \rangle / \bar{u} = 0.25\%$. The current intensity levels are also comparable to measurements acquired by Wlezien et al.[14] again using the wall-mounted probe struts. Quest[5] reported ETW massflux intensity data using a strut-mounted conical hot-film probe of $\langle m' \rangle / \bar{m} \approx 0.12\%$ to 0.25%, consistent with most of our data. No information was found on the high-pass filter setting but the data includes frequencies up to 20 kHz. However, the hot-wire spectrum he presented rolls off significantly by 2 kHz.

As mentioned previously, the large $\langle m' \rangle / \bar{m}$ levels in Fig. 17 are partly due to intense low-frequency energy. Three data points (test points 2356, 2418 and 2420) corresponding to $M = 0.85$ are identified in Fig. 17c where the intensity at pt 2420 is more than 3 times the other values. Points 2356 and 2418 were acquired at the same tunnel conditions but at a higher Reynolds number than point 2420. The time histories corresponding to those data points are shown in Fig. 19a. Data for point 2418 were acquired at a higher sample rate of 192 kHz and a frequency bandpass of $0.1 \text{ Hz} \leq f \leq 75$ kHz. The low-frequency oscillations in the time trace for point 2420 are clearly evident. The associated PSD's are presented in Fig. 19b along with a $-5/3$ curve to depict decaying screen turbulence. The PSD's do follow approximately a $-5/3$ decay between about $f = 200$ to 1500 Hz. Note also that the increase in the intensity level for pt 2420 is due to an increase in the overall spectral energy, though the differences are larger for

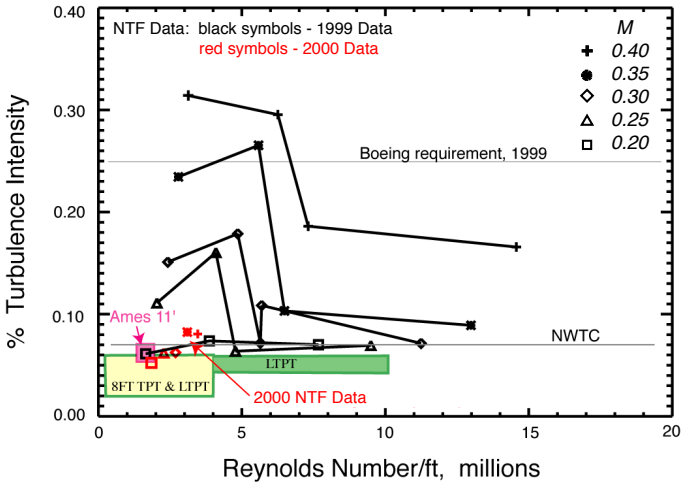

Figure 18: NTF turbulence data acquired in 1999 & 2000 along with selected data acquired in three other NASA facilities. Plot reproduced with permission of McGinley et al.[13]

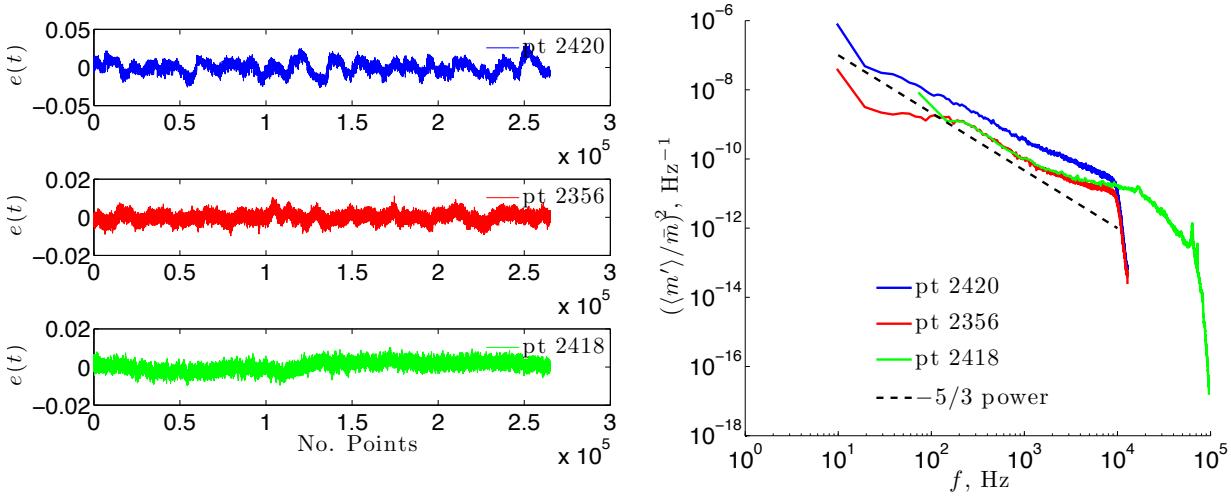

(a) Time histories

(b) Power spectral densities

Figure 19: Hot-wire data at M = 0.85 in the form of (a) time histories and (b) PSD's for points 2420, 2356 and 2418 identified in Fig. 17c.

$f < 100$ Hz. The $\langle m' \rangle / \bar{m}$ values for points 2418 (75 kHz BW) and 2356 (10 kHz BW) are 0.16% and 0.14%, respectively. This is evidence that in a facility where the turbulence behaves as decaying screen turbulence, the high-pass filter setting will not affect substantially the standard deviation provided the bandwidth is large enough to capture several decades drop in the spectrum. On the other hand, consider point 2420 which has substantial low-frequency spectral energy. The $\langle m' \rangle / \bar{m}$ values are 0.50% and 0.34% for high-pass filter settings of 0.1 Hz and 10 Hz, respectively. So with the 10-Hz setting, we only get about 68% of the $\langle m' \rangle / \bar{m}$ value.

Following a similar process as was done to examine the spatial variations of the unsteady pressure measurements, we plot $\langle m' \rangle / \bar{m}$ versus ϕ for the various hot-wire channels. In the plots to follow, two to four channels of hot-wire output will be presented and this is because sensors were lost during or prior to the roll polars. Fig. 20a shows the massflux intensity as a function of roll angle for an air-mode condition and excursions (as large as $\sim 6\times$baseline value) can be seen from the baseline value of $\langle m' \rangle / \bar{m} \approx 0.08\%$. The location of each sensor is provided in the plot legend. Note that HW4 is on the center of rotation of the rake and on the test-section centerline. In addition, the massflux intensity derived from the acoustic measurements are included in this figure for comparison. These measurements are marginally larger than the baseline values obtained by the wire. It is clear from these measurements (compare HW3 with P_t, P_s) at the same radial distance, r, that the acoustic measurements are relatively insensitive to the massflux excursions measured by the wire. The reason for this insensitivity is unclear. The mean total temperature measurements obtained with the RTD probes do not show any spatial temperature variations consistent with these excursions to influence the hot-wire output. Secondly, the mean hot-wire outputs, ($\bar{m} = \bar{\rho}\bar{u}$), also do not show any spatial variations consistent with the excursions that would be indicative of potential shear layers. It is possible that our inability to measure any discernible mean flow gradients of $\bar{T}_t$ and $\bar{m}$ may be due to a lack of sensitivity of our sensors to small flow gradients. These large excursions are indeed problematic for transition sensitive testing. On the positive side, if the sources of these disturbances are eliminated or their impact mitigated, the baseline values are very close to those recommended by the NWTC. The largest excursions measured are those presented in this figure. The sources of these excursions do not appear to be associated with the wagon wheel (i.e., the spokes) since the excursions are not aligned with the roll angle ϕ. The larger the radii, the more peaks appear. The same data are replotted in Fig. 20b but versus the projected span location, $r \cos\phi$, where positive span values refer to the starboard side of the rake at $\phi = 0°$. The peak alignments are discernible in this plot and suggest that the vertical plates used to join the individual cooling coil sections are the likely sources (refer back to Fig. 9b). The hot-wire probe, HW4, on the centerline is located downstream of one of these vertical plates; as a consequence, the measured intensities are large for this sensor. These vertical structures have blunt trailing edges that are at least several centimeters wide. In fact, fairings were designed (NTF drawings dated 1979) for the trailing edges but for reasons unknown to the authors, these fairings were not installed.

Two additional plots at $M = 0.2$ and $M = 0.85$ are shown in Fig. 21 for air-mode conditions. At $M = 0.2$ as seen in Fig. 21a, the maximum massflux intensities are approximately 50% the maximum values for $M = 0.4$. An increase in $\langle m' \rangle / \bar{m}$ is observed for the higher Mach numbers as demonstrated in Fig. 21b. The massflux intensities derived from the pressure field show very good agreement in general with the hot-wire results except for the low Mach number of $M = 0.2$ where there is significant statistical variation in the acoustic measurements (refer to Section III.A).

We now examine similar data at cryogenic conditions for higher Reynolds numbers to determine if this flow disturbance anomaly persists at these conditions. The data are presented in Fig 22 for three Mach numbers. The most important observation is that there is no evidence of the flow anomaly observed for air-mode conditions at the cryogenic conditions. Even for the cryogenic condition at relatively low Reynolds number in Fig. 22a, these excursions are not apparent – just a modest intensity increase in HW3 near $\phi \approx \pm 180°$. The other general observation is that there is an increase in the baseline levels for the cold conditions versus warm conditions. The intensity levels show very little spatial variation in the test section with a nominal value of $\langle m' \rangle / \bar{m} \approx 0.2\%$. As noted earlier, the massflux intensities derived from the pressure measurements are large for $M = 0.2$, in particular for the cryogenic condition shown in Fig. 22b (note the ordinate scale change). For the higher Reynolds numbers in Figs.22c and 22d, the $\langle m' \rangle / \bar{m}$ levels appear to measurably improve and the comparison is good between the different massflux measurements. These results are very encouraging as one of the NTF's primary functions is to conduct flight-relevant aerodynamic testing on sub-scale models for transport-type configurations, and it is in this flow regime that the flow disturbance field performs well.

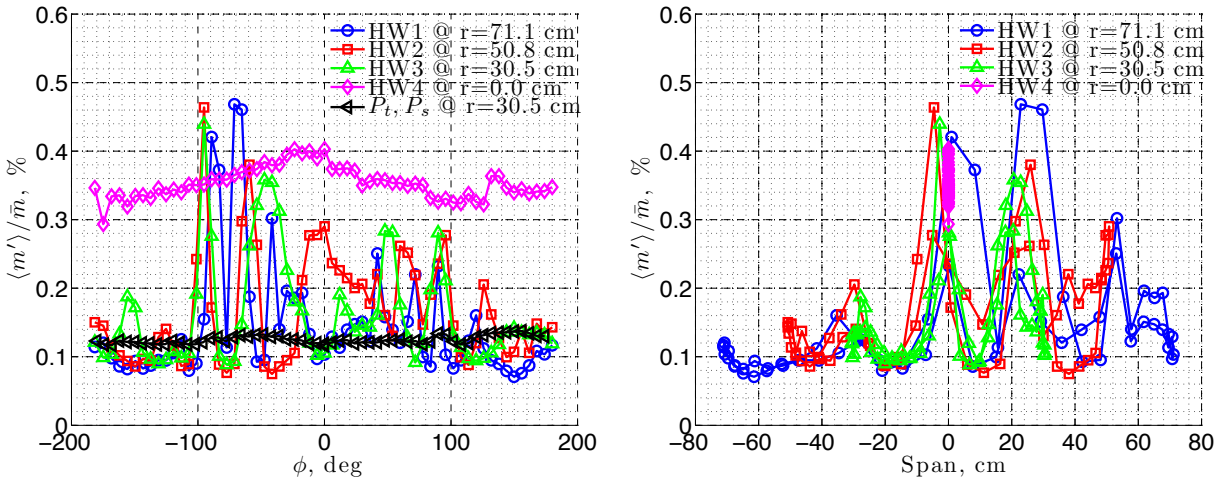

(a) Massflux intensity versus roll angle

(b) Massflux intensity versus projected span

Figure 20: Spatial distribution of $\langle m' \rangle / \bar{m}$ versus (a) roll angle and (b) span location for $T_t = 322$ K, $M = 0.4$, and $Re/m = 30.9 \times 10^6$.

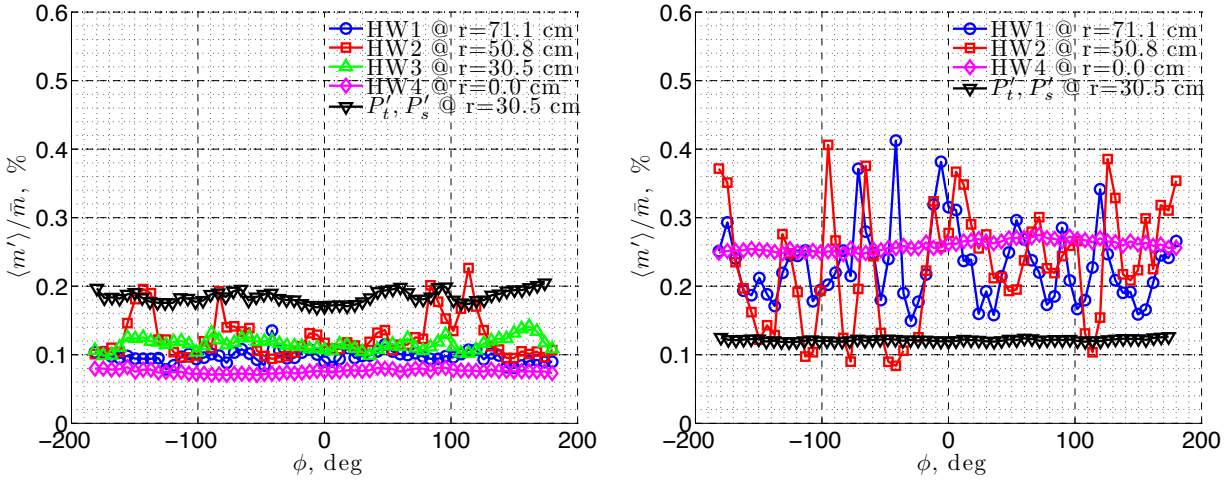

(a) $M = 0.2$, $Re/m = 16.3 \times 10^6$

(b) $M = 0.85$, $Re/m = 26.0 \times 10^6$

Figure 21: Spatial distribution of $\langle m' \rangle / \bar{m}$ versus roll angle for additional air-mode conditions ($T_t = 322$ K) at (a) $M = 0.2$ and (b) $M = 0.85$.

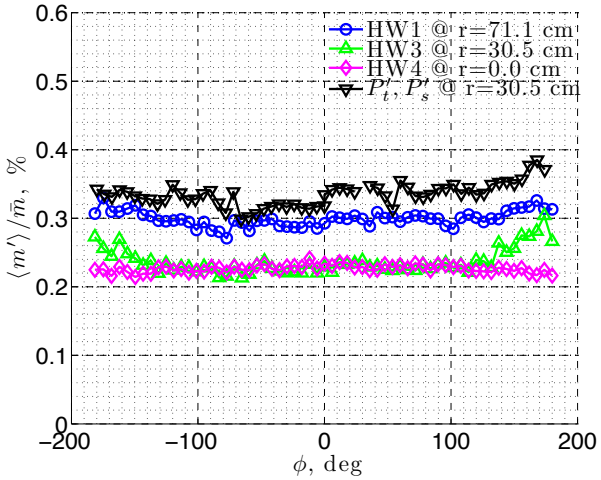

(a) $M = 0.2$, Re/m= 37.6×10^6, $T_t = 172$ K

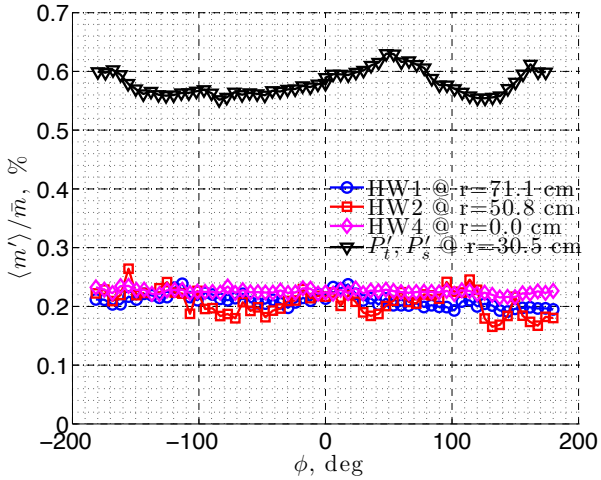

(b) $M = 0.2$, Re/m= 65.6×10^6, $T_t = 116$ K

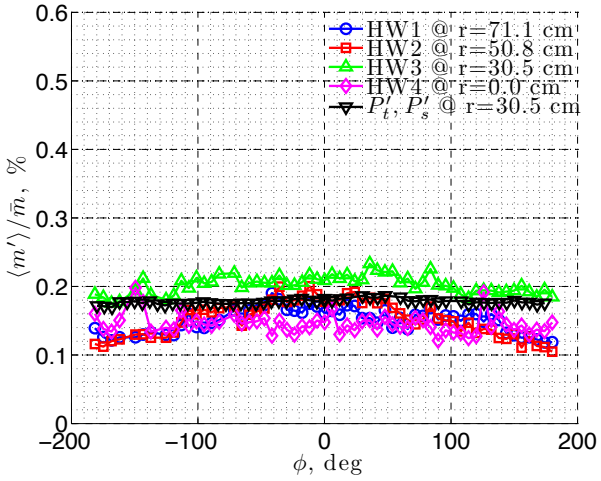

(c) $M = 0.4$, Re/m= 104.5×10^6, $T_t = 116$ K

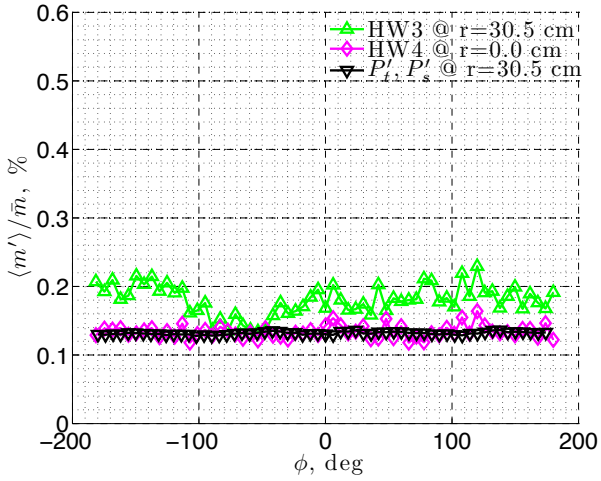

(d) $M = 0.85$, Re/m= 108.5×10^6, $T_t = 116$ K

Figure 22: Spatial distribution of $\langle m' \rangle / \bar{m}$ versus roll angle for cryogenic-conditions at (a) M = 0.2, (b) M = 0.2 (note the scale change), (c) M = 0.4 and (d) M = 0.85.

IV. Summary

A fairly comprehensive study was conducted in the NTF to ascertain the unsteady disturbance field in the tunnel's test section for both air and nitrogen operational modes by utilizing the NTF survey rake. The primary unsteady sensors used to acquire the data were unsteady pressure sensors and hot-wire sensors. The cryogenic mode was found to be a harsh environment for the hot wires in terms of survivability and repair constraints. An added benefit of this study was the collection of hot-wire anemometry data over a wide range of wire Reynolds numbers, $20 < Re_t < 900$. With this data in hand, we were able to assess from our vantage point the best approach on how to reduce the transonic hot-wire data. To our knowledge, there are no other NTF hot-wire results documented for the Reynolds numbers achieved in this study, $Re/\mathrm{m} \approx 220 \times 10^6$ ($Re/\mathrm{ft} \approx 67 \times 10^6$).

The measurements of $\langle P_s' \rangle / q$ and $\langle m' \rangle / \bar{m}$ ($\approx \langle u' \rangle / \bar{u}$ for $M < 0.4$) are consistent with warm and cryogenic results acquired using fixed sidewall-mounted probes by both McGinley et al.[13] and later by Wlezien et al.[14] We measured substantial spatial variation of the unsteady disturbance field for air-mode conditions only. The largest massflux intensities measured were approximately 6 times the baseline values or one order of magnitude larger than the NWTC recommended value. The sources of this flow anomaly are believed to be shedding from the blunt trailing edges of the vertical plates separating the cooling coil packs. Remnants of these fluid structures persist through the turbulence treatment screens into the test section. These vortical disturbances can be very problematic for transition sensitive studies as these fluid structures can wrap around the leading edge of a test article inducing Klebanoff modes or local streaky structures. This can lead to premature laminar-to-turbulent breakdown induced by streak instabilities. This disturbance anomaly, observed only for low Reynolds number air-mode conditions, needs to be resolved before future transition sensitive testing is conducted on a test article susceptible to this type of laminar breakdown. The disturbance flow anomaly was not observed at high Reynolds number cryogenic conditions and for the conditions tested, the disturbance field is relatively spatially homogeneous. In fact, the NTF appears to have improved performance at flow conditions relevant to transport configurations, i.e., high Reynolds number and transonic Mach numbers. The measurements of $\langle P_s' \rangle / q$ and $\langle m' \rangle / \bar{m}$ are comparable to results reported for ETW by Quest,[5] though his high-pass filter settings were not reported. Our results also support a recent collaborative test by Boeing and NASA (Crouch et al.[15]) on a transonic wing at cryogenic conditions where the turbulence intensity was indirectly estimated to be $\%Tu \approx 0.24$ using the method of Mack.[16] Crouch et al. concluded that the 0.24% turbulence intensity is sufficient to conduct laminar-flow testing in the absence of bypass transition. Our direct measurements support these turbulence levels and we support the conclusion that the NTF disturbance levels at cryogenic conditions are acceptable for laminar-flow testing. The information provided in this document – intensity levels, spectral content, location and spatial variation – can be used as a guide to determine the impact of the reported fluctuating results, if any, on their desired performance data.

V. Acknowledgements

This work was supported by the Airframe Technology Subproject in the Environmentally Responsible Aviation Project Office without which this study would not be possible. The authors thank the entire NTF support staff for their work and long hours invested for the test program. Special thanks to the lead test engineer Joshua Revenaugh and to James "Monty" Montgomery for his diligent and painstaking efforts to replace the hot-wire sensors in-situ in a less than ideal environment. Wayne Geouge and Mark Roth are recognized for their ingenious craftsmanship and creative ideas related to the assembly of the hot-wire probes and unsteady pressure probes. And finally, the authors thank the members of Flow Physics and Control Branch for the many useful discussions and exchange of ideas throughout the test program.

References

[1]Fuller, D. E., "Guide for Users of the National Transonic Facility," NASA-TM-83124, July 1981.

[2]Campbell, J. F., "The National Transonic Facility - A Research Perspective," AIAA Paper 84-2150, Aug. 1984.

[3]Wahls, R. A., "The National Transonic Facility: A Research Retrospective (Invited)," AIAA Paper 2001-0754, Jan. 2001.

[4]Bissett, O. W. and Hudson, C. M., "Selected Major Modifications to the National Transonic Facility," AIAA Paper 2009-419, Jan. 2009.

[5]Quest, J., "ETW - High Quality Test Performance in Cryogenic Environment," AIAA Paper 2000-2206, June 2000.

[6]Green, J. and Quest, J., "A Short History of the European Transonic Wind Tunnel ETW," *Progress in Aerospace Sciences*, Vol. 47, No. 5, July 2011, pp. 319–368.

[7]Collier, F., Thomas, R., Burley, C., Nickol, C., Lee, C.-M., and Tong, M., "Environmentally Responsible Aviation - Real Solutions for Environmental Challenges Facing Aviation," 27TH ICAS, Aug. 2010.

[8]Bezos-O'Connor, G. M., Mangelsdorf, M. F., Maliska, H. A., Washburn, A. E., and Wahls, R. A., "Fuel Efficiences Through Airframe Improvements," AIAA Paper 2011-3530, June 2011.

[9]Joslin, R. D., "Overview of Laminar Flow Control," NASA/TP-1998-208705, Oct. 1998.

[10]Whites, R. C., Sudderth, R. W., and G, W. W., "Laminar Flow Control on the X-21," *Astronautics and Aeronautics*, Vol. 4, July 1966, pp. 38–43.

[11]Boeing Commercial Airplane Company, "Hybrid Laminar Flow Control Study - Final Technical Report," NASA-CR-165930, Oct. 1982.

[12]Igoe, W. B., "Analysis of Fluctuating Static Pressure Measurements in the National Transonic Facility," NASA TP-3475, March 1996.

[13]McGinley, C. B., Melton, L. P., and Neuhart, D. H., "Unpublished NTF Flow Quality Measurements Acquired in 1999 and 2000," Personal Communication.

[14]Wlezien, R., White, R., Eppink, J., Liu, S., and Krause, J., "NTF Flow Quality Characterization for Laminar Flow Testing," Final Report for Task Order No. NNL08AM27T (072D3), Sept. 2009.

[15]Crouch, J. D., Sutanto, M. I., Witkowski, D., Watkins, A. N., Rivers, M. B., and Campbell, R. L., "Assessment of the National Transonic Facility for Natural Laminar Flow Testing," AIAA Paper 2010-1302, Jan. 2010.

[16]Mack, L. M., "Transition Prediction and Linear Stability Theory," AGARD Laminar-Turbulent Transition, CP-224, 1977.

[17]Foster, J. M. and Adcock, J. B., "User's Guide for the National Transonic Facility Research Data System," NASA-TM-110242, April 1996.

[18]Seraudie, A., Archambaud, J. P., and Mignosi, A., "Measurement Techniques Developed for Cryogenic Field in T2 Transonic Wind Tunnel," AGARD Advanced Aerodynamic Measurement Technology, CP-601, Sept. 1997.

[19]Kovásznay, L., "The Hot-Wire Anemometer in Supersonic Flow," *Journal of the Aeronautical Sciences*, Vol. 17, No. 9, Sept. 1950, pp. 565–572.

[20]Dewey, C. F., "A Correlation of Convective Heat Transfer and Recovery Temperature Data for Cylinders in Compressible Flow," *International Journal of Heat and Mass Transfer*, Vol. 8, 1965, pp. 245–252.

[21]Behrens, W., "Total Temperature Thermocouple Probe Based on Recovery Temperature of Circular Cylinder," *International Journal of Heat and Mass Transfer*, Vol. 14, 1971, pp. 1621–1630.

[22]King, L. V., "On the Convection of Heat from Small Cylinders in a Stream of Fluid: Determination of the Convection Constants of Small Platinum Wires with Applications to Hot-Wire Anemometry," *Philosophical Transactions of the Royal Society A*, Vol. 214, Nov. 1914, pp. 373–432.

[23]Morkovin, M. V., "Fluctuations and Hot-Wire Anemometry in Compressible Flows," AGARDograph 24, Nov. 1956.

[24]Laufer, J. and McClellan, R., "Measurements of Heat Transfer from Fine Wires in Supersonic Flows," *Journal of Fluid Mechanics*, Vol. 1, No. 3, 1956, pp. 276–289.

[25]Smits, A. J., Hayakawa, K., and Muck, K. C., "Constant Temperature Hot-Wire Anemometer Practice in Supersonic Flows Part 1: The Normal Wire," *Experiments in Fluids*, Vol. 1, April 1983.

[26]Rose, W. C. and McDaid, E. P., "Turbulence Measurement in Transonic Flow," *AIAA Journal*, Vol. 15, No. 9, Sept. 1977, pp. 1368–1370.

[27]Horstman, C. C. and Rose, W. C., "Hot-Wire Anemometry in Transonic Flow," NASA-TM-X-62495, Dec. 1975.

[28]Rong, B. S., Tan, D. K. M., and Smits, A. J., "Calibration of the Constant Temperature Normal Hot-Wire Anemometer in Transonic Flow," Princeton University Report MAE-1696, April 1985.

[29]Johnson, P. C. and Crouch, J. D., "Flow Quality Requirements for Laminar Flow Testing," NAS3-27330, Doc. No. DB-1-026, Aug. 1995.

[30]NWTC Government/Industry Team, "National Wind Tunnel Complex (NWTC) Final Report," NASA CR-198491, June 1996.

[31]Bobbitt, C. J. and Everhart, J., "Status of the National Transonic Facility Characterization (Invited) ," AIAA Paper 2001-0755, Jan. 2001.

[32]Kilgore, W. A., Balakrishna, S., and Butler, D. H., "Reduction of Tunnel Dynamics at the National Transonic Facility (Invited)," AIAA Paper 2001-1162, Jan. 2001.